Thesis for the degree of Licentiate of Philosophy

Dynamics and Reactivity of Cu-species in Cu-CHA for NH_3-SCR

Joachim Dithmer Bjerregaard

Department of Physics
CHALMERS UNIVERSITY OF TECHNOLOGY
Göteborg, Sweden 2025

Dynamics and Reactivity of Cu-species in Cu-CHA for NH_3-SCR
Joachim Dithmer Bjerregaard

© Joachim Dithmer Bjerregaard, 2025

Department of Physics
Chalmers University of Technology
SE-412 96 Gothenburg
Sweden
Telephone +46 31 772 1000

Cover: Illustration of the reaction mechanism for NH_3-SCR over Cu-CHA and the effect of SO_2

Typeset in LaTeX
Printed at Chalmers Digitaltryck
Göteborg, Sweden 2025

Dynamics and Reactivity of Cu-species in Cu-CHA for NH_3-SCR

Joachim Dithmer Bjerregaard
Department of Physics
Chalmers University of Technology

Abstract

Copper exchanged chabazite (Cu-CHA) is a state-of-the-art catalyst for deNO$_x$ via ammonia assisted selective catalytic reduction (NH_3-SCR) in lean burn engines, owing to its good low-temperature activity, and high hydrothermal stability. One challenge for Cu-CHA is, however, the sensitivity to sulfur species, which are present in the exhaust gas. Even at small concentrations, sulfur accumulates in the catalyst leading to a loss in activity and a reduction in the operational lifetime. A better understanding of the NH_3-SCR activity and sulfur poisoning is important for the development of catalysts with high activity that are sulfur resistant.

In this thesis, density functional theory (DFT) calculations are used to study the mechanism for the sulfur poisoning of Cu-CHA during NH_3-SCR conditions, with a focus on low-temperature deactivation. It is suggested that SO_2 reacts with $[Cu_2(NH_3)_4O_2]^{2+}$ resulting in accumulation of ammonium bisulfate species inside the chabazite cage. This hinders the pairing of $[Cu(NH_3)_2]^+$ complexes, which is needed for adsorption of O_2, leading to a loss in activity. At high temperatures, it is proposed that SO_2 and SO_3 primary react with ZCuOH and Z_2CuOOCu complexes, forming stable copper sulfur species, with SO_3 forming Cu sulfates with highest stability. The combination of DFT with micro-kinetic modeling has, moreover, been used to investigate H_2 temperature programmed reduction (H_2-TPR) profiles to aid the interpretation of experimental H_2-TPR profiles.

Given the importance of $[Cu(NH_3)_2]^+$ diffusion for the O_2 adsorption and subsequently reduction of NO, a machine learning force field (ML-FF) has been constructed that is trained with DFT data. The use of ML-FF makes it possible to simulate system sizes and timescales inaccessible to conventional ab initio molecular dynamics (AIMD). The effect of zeolite composition on the mobility and pairing of $[Cu(NH_3)_2]^+$ complexes is studied using different analysis tools. It is found that a high Cu/Al and low Si/Al ratio enhance the pairing of $[Cu(NH_3)_2]^+$ complexes.

Keywords: Cu-CHA, NH_3-SCR, Sulfur Deactivation, Diffusion, DFT, Machine Learning Force Field

Publications

This thesis is based on the following appended papers:

I. On the Interpretation of H_2-TPR from Cu-CHA using First-Principles Calculations
J. D. Bjerregaard, J. Han, D. Creaser, L. Olsson, and H. Grönbeck
The Journal of Physical Chemistry C, In revision

II. Mechanism for SO_2 Poisoning of Cu-CHA during Low-Temperature NH_3-SCR
J. D. Bjerregaard, M. Votsmeier and H. Grönbeck
The Journal of Catalysis, 2023, 417, 497-506

III. Effect of SO_2 and SO_3 Exposure to Cu-CHA on Surface Nitrate and N_2O Formation for NH_3-SCR
J. Han, J. D. Bjerregaard, H. Grönbeck, D. Creaser, L. Olsson
In manuscript

IV. Effect of Aluminum Distribution on the Diffusion and Pairing of $[Cu(NH_3)_2]^+$ Complexes in Cu-CHA
J. D. Bjerregaard, M. Votsmeier and H. Grönbeck
In manuscript

My contributions to the publications

Paper I
I performed all the calculations and programmed the micro-kinetic model. I wrote the first draft of the paper, which was finalized together with my co-authors.

Paper II
I performed all the calculations. I wrote the first draft of the paper, which was finalized together with my co-authors.

Paper III
I performed all the calculations. I wrote the draft for the theoretical part of the manuscript. The manuscript was finalized by all co-authors

Paper IV
I performed all the calculations. I wrote the first draft of the manuscript, which was finalized together with my co-authors.

Contents

1 **Introduction** **1**
- 1.1 NO_x Emissions 1
- 1.2 Heterogeneous Catalysis 2
- 1.3 NH_3-SCR 3
- 1.4 Catalyst Deactivation 5
- 1.5 Objectives 6

2 **Electronic Energy** **9**
- 2.1 The Schrödinger Equation 9
- 2.2 Density Functional Theory 9
  - 2.2.1 Exchange Correlation Functionals 11
  - 2.2.2 Basis Sets and Pseudopotentials 12
  - 2.2.3 Bader Charge Analysis 13
- 2.3 Parameterization of Energy 13
  - 2.3.1 Force-Field 13
  - 2.3.2 Machine Learning Force-Fields 14
  - 2.3.3 Long-range Interactions 15
  - 2.3.4 Neural Network 15

3 **Towards Elevated Pressure and Temperature** **17**
- 3.1 Optimization 17
- 3.2 Transition State Search 18
- 3.3 Vibrations 18
- 3.4 Statistical Mechanics 19
- 3.5 Molecular Dynamics 20
- 3.6 Enhanced Sampling Technique 21
  - 3.6.1 Metadynamics 21
- 3.7 Micro-Kinetic Modeling 22

4 **Sulfur Poisoning during NH_3-SCR** **25**
- 4.1 State of Cu during Operating Conditions 25
- 4.2 Sulfur Poisoning 26
  - 4.2.1 Low-temperature Deactivtion 27
  - 4.2.2 High-temperature Deactivation 27

5 **Mobility of $[Cu(NH_3)_2]^+$ Complexes** **31**
- 5.1 Pair Correlation Function 31

5.2 Mobility and Pairing 32

6 Conclusions and Outlook 35

Acknowledgments 37

Bibliography 39

1

Introduction

Since the advent of industrialization, humans have emitted large quantities of greenhouse and toxic gases into the atmosphere. Emissions of gases such as CO_2 and CH_4 contribute to the greenhouse effect, which, leads to rising temperatures globally.[1] Simultaneously, there has been an increase in pollutants like NO_x (x=1,2), SO_2, CO, and particulate matter (PM), affecting the local air quality. In fact, 99 % of the world population today, breathes air that surpasses the guidelines set by the World Health Organization (WHO),[2] thus, there is an urgent need for reducing air pollution. One of the main sources of NO_x is combustion processes from petrol or diesel-powered vehicles and power plants. Biogenic sources of NO_x include lighting and volcanic activities, although they are not as important as anthropogenic emissions.[3] In the EU, the road transport sector is the largest source of NO_x, accounting for 39 % of the total emissions.[4] The second largest source is the energy production and distribution sector emitting 16 % of the total NO_x emissions.[4] Fortunately, large improvements have been made regarding NO_x emissions during the last decades. The NO_x emissions from transport in the EU has decreased by 53 % with respect to the 1990-level,[4] which is largely attributed to the development of new catalytic aftertreatment systems for NO_x control.[5] However, there is a continuous need to improve catalytic techniques for NO_x control, due to the increasingly stringent regulations concerning emissions from fuel engines.

1.1 NO_x Emissions

NO_x have negative health effects, such as respiratory and lung problems,[2] however many of the negative effects associated with NO_x originate from the reaction of NO_x with other species in the atmosphere. Both NO and NO_2 are reactive molecules with short lifetimes of around 4 days.[3] NO_x is a precursor for the formation of tropospheric O_3 and can react with volatile organic compounds (VOC), which can lead to the formation of smog.[6] Furthermore, NO_2 can react with OH radicals in the atmosphere forming nitric acid[7] according to:

$$NO_2 + OH \longrightarrow HNO_3 \tag{R1}$$

Nitric acid HNO_3, is soluble in H_2O and may contribute to acid rain, causing damage to the ecosystem.[8] Emission control strategies can be designed to reduce the formation of NO_x directly from the source or by removing NO_x once it is formed. NO_x abatement methods may include physical processes such as filters that adsorb

NO_x for which typically active carbon is used or a catalyst that can chemically react with NO_x, forming the harmless gases N_2 and H_2O.[3] The use of a catalyst is the method of choice for NO_x control of fuel-powered vehicles. For gasoline cars, the three-way-catalyst (TWC) is used thanks to its ability to efficiently remove NO_x, CO, and hydrocarbon (HC) simultaneously. NO_x is reduced to N_2 and H_2O, while CO and HC are oxidised to CO_2 and H_2O. The TWC is typically based on Pt, Pd, and Rh nanoparticles supported on a metal oxide such as Al_2O_3.[9] Promoters in the form of metal oxides with high oxygen capacity, such as CeO_2 are also added. TWC has the limitation that it must be operating under stoichiometric conditions, which exclude the use of TWC in lean burn engines, where there is an excess of O_2. The use of lean burn engines provides a better fuel economy compared to stoichiometric engines.[10] To remove NO_x from lean burn engines ammonia assisted selective catalytic reduction (NH_3-SCR) is typically used. In this technology NH_3 is dosed over a catalyst, that reacts with NO_x forming N_2 and H_2O. Zeolite- or vanadium-based catalyst is commonly used for NH_3-SCR since they show high activity and selectivity towards reducing NO_x to N_2 and have at the same time a good hydrothermal stability.[11]

1.2 Heterogeneous Catalysis

A catalyst is defined as a material that can increase the rate of a reaction without changing the standard Gibbs energy.[12] A catalyst is ideally not, consumed during the reaction, hence only small amounts of catalyst are required. Catalysts are a fundamental part of modern society and it is estimated that 85 % of all chemical products are produced using a catalyst.[13] Catalysts are generally divided into homogeneous, enzymatic, and heterogeneous catalysts. In homogeneous catalysts, the reactants and products are in the same phase as the catalyst.[14] Enzymatic catalysts are enzymes used in biochemical reactions. In heterogeneous catalysis, the reactant and products have a different phase from the catalyst. The catalyst is typically in solid phase while the reactants and products are in gas phase. The advantage of using heterogeneous catalysts is the ease of separating catalysts and products, however, they typically have lower selectivity compared to homogeneous catalysts.[14] The role of a catalyst on the potential energy landscape is illustrated in Figure 1.1. Two pathways are shown that have the same reactants and products. However, the landscape connecting the initial and final state are different. Typically for surface reactions, the use of a catalyst introduces several intermediates along the reaction coordinate. These intermediates could be the adsorption and desorption processes and the different steps of the surface reactions. The non-catalyzed reaction has one high activation barrier, while the catalyzed reaction has many lower activation energies, which increases the rate of the reaction as given by the Arrhenius equation:

$$r = Ae^{-E_a/k_BT} \tag{1.1}$$

The rate scales experimentally with the barrier, E_a. A is the pre-expotential factor, k_B is the Boltzmann constant and T is the temperature. One role of the catalyst is to assemble the reactants, so they are close and can react with each other. Even though

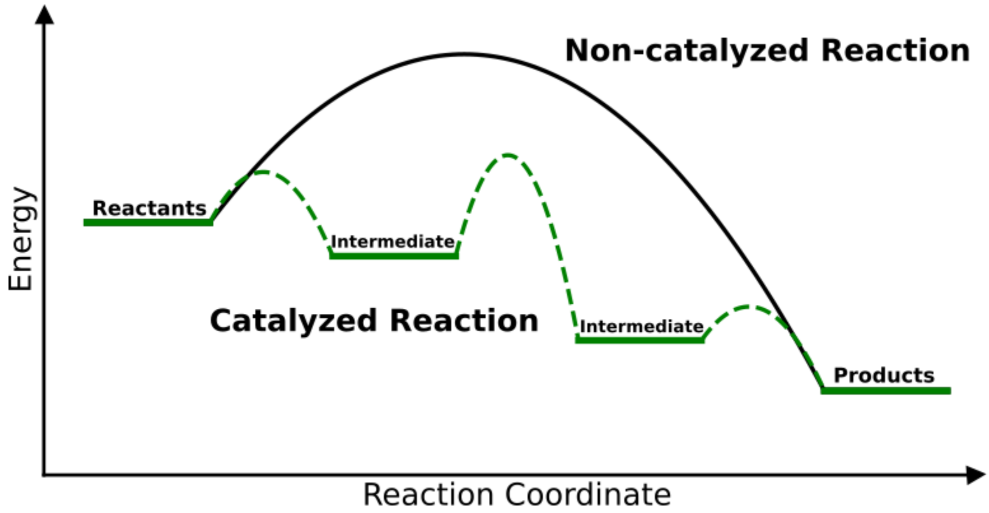

Figure 1.1: Potential energy diagram, for a catalyzed reaction and non-catalyzed reaction.

the catalyst is not consumed during the reaction, it may lose activity over time, due to deactivation. Examples of deactivation processes are poisoning of the active site by containments in the gas-feed, thermal degradation if the catalyst is operated at high temperature, or fouling, which is physical deposition onto the catalyst, such as carbon or coke.[15] Hence, a catalytic process should aim at having both a high activity to the desired product and a good stability of the catalyst.

1.3 NH_3-SCR

The NH_3-SCR treatment systems in diesel-powered vehicles, use urea, which upon heating releases NH_3. NH_3 can react with NO in presence of O_2 through the so-called, standard SCR reaction.

$$4\,NH_3 + 4\,NO + O_2 \longrightarrow 4\,N_2 + 6\,H_2O \tag{R2}$$

The stoichiometry between NH_3 and NO is one, and the presence of O_2 is required for the abstraction of the hydrogen atoms. A catalyst suitable for NH_3-SCR should have redox properties to allow for O_2 adsorption and, be able to adsorb and facilitate NO and NH_3 coupling. NO is the main component of NO_x emissions in diesel combustion.[16] However, in presence of NO_2, the SCR reaction can proceed according to the so-called fast SCR.

$$2\,NH_3 + NO + NO_2 \longrightarrow 2\,N_2 + 3\,H_2O \tag{R3}$$

Side reactions that can occur simultaneously with the desired SCR-reactions, such as oxidation of NH_3 and NO, need to be suppressed. One important side reaction is the formation of N_2O.

$$2\,NH_3 + 2\,NO + O_2 \longrightarrow N_2 + N_2O + 3\,H_2O \tag{R4}$$

N_2O is a potent greenhouse gas, and this side reaction should be avoided. Common catalysts for NH_3-SCR include vanadium-based and zeolite-based materials.[11] For vanadium-based catalyst, TiO_2 is normally used as support, thanks to its high SO_2 resistance and good dispersion of V_2O_5.[17] However TiO_2 can undergo an unwanted phase transition from anatase to rutile during high temperatures and a promotor such as WO_3 is often added to stabilize the catalyst.[18] The addition of WO_3 enhances at the same time, the low-temperature activity.[18] A drawback with vanadium-based catalysts is that VO_x species are volatile, which, poses a health risk.[19] The standard SCR is believed to occur as a redox reaction on V^{+5} sites in a Mars-van Krevelen type of mechanism[20] where NH_3 and NO reduces the active site to V^{+4}. V^{+4} is then reoxidized by O_2 back to V^{+5}.

Zeolites are hydrated crystalline aluminum silicates, which can be found in nature or can be synthesised.[21] Zeolites are composed of tetrahedral TO_4 sites where T is Si or Al. Pure silicates (SiO_2) do not contain any charges as silicon is tetravalent. However, as Al is trivalent, it requires a balancing counter ion, which could be a proton. In natural zeolites, the counter ion is typically Na^+ or K^+.[21] It is possible to do an ion exchange and this is commonly done with either Cu or Fe.[22] Zeolites consist of connected cages, which are the size of molecules, giving a high size selectivity and unique properties. As of today, there are 255 zeolites with different frameworks as documented by the International Zeolite Association (IZA).[23] Each zeolite framework is assigned a 3-letter combination, with BEA and CHA being two zeolites that are commonly used for NH_3-SCR. BEA is classified as a large pore-size zeolite with the largest ring consisting of 12 Si atoms. BEA has shown good tolerance against sulfur,[24] however, it suffers from thermal degradation[25] and hydrocarbon poisoning.[26] CHA is a small pore zeolite with the structure illustrated in Figure 1.2. Chabazite consists of two cages, a small cage made up of four- and six-membered rings and a large cage, consisting of four- six- and eight-membered rings. Cu exchanged chabazite (Cu-CHA) zeolites are known to have good hydrothermal stability,[27] with a good low-temperature activity to the SCR-reaction[28] and is the catalyst studied in this thesis.

The low-temperature NH_3-SCR mechanism has been extensively studied during the last few years.[29–31] The active site in Cu-CHA for low-temperature NH_3-SCR is NH_3 solvated copper complexes $[Cu^+(NH_3)_2]^+$. $[Cu^+(NH_3)_2]^+$ are mobile complexes that can diffuse between the CHA-cages and if two complexes are paired in the same cage, they can adsorb O_2 forming a peroxo complex $[Cu_2^{2+}(NH_3)_4O_2]^{2+}$. NH_3 and NO can couple over the complex forming HONO and H_2NNO, which are connected to N_2 and H_2O. The NO-NH_3 coupling[30,31] reduces Cu back to $[Cu^+(NH_3)_2]^+$. The reaction is a redox-cycle where Cu changes between oxidation states +1 and +2. The mechanism for the high temperature is less well known but is believed to occur over framework-bound Cu.

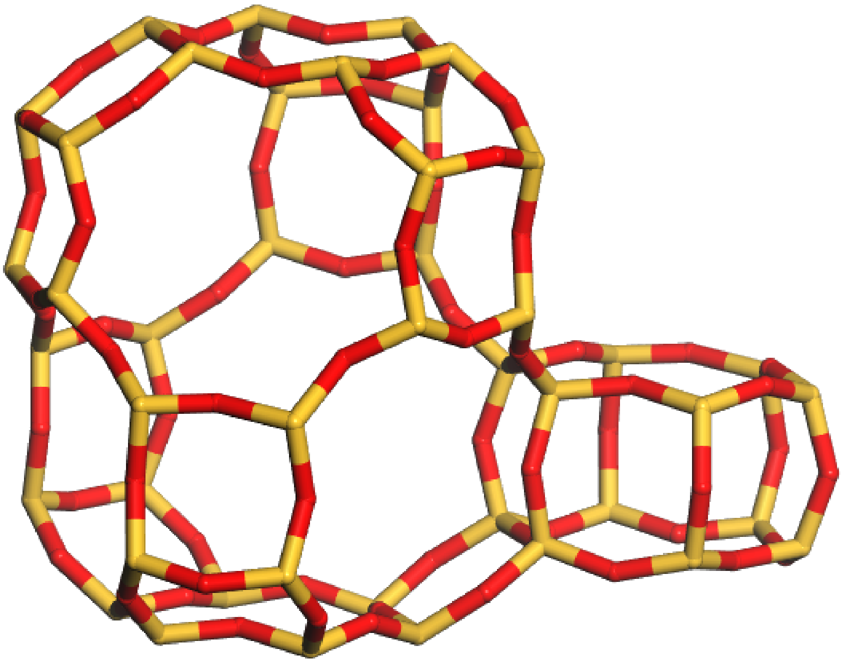

Figure 1.2: The two cages, that make up the Chabazite structure. Atomic color codes: Si (yellow) and O (red).

1.4 Catalyst Deactivation

Deactivation of Cu-CHA is a significant challenge, as it impacts the activity and life time of the catalyst. The deactivation of a catalyst is closely related to the chemicals and temperature that the catalyst is exposed to. Exhaust gas contains various contaminants derived from the engine and fuel additives, that may deactivate Cu-CHA.[32] The possible contaminants include phosphor, alkali metals, hydrocarbon, and sulfur. Phosphor has been suggested to form Cu-phosphate species that deactivate the catalyst[33,34] and may become a significant problem in the future due to the introduction of biomass fuels.[33] Hydrocarbons formed during incomplete combustion, cause significant deactivation in large pore zeolite such as BEA. However, a small pore zeolite such as Cu-CHA is generally not poisoned by the larger hydrocarbons[35] such as dodecane, $C_{12}H_{26}$, due to the small ring size preventing larger molecules from entering. Smaller hydrocarbons like C_3H_6 do deactivate the catalyst, but only slightly and in the medium temperature range (200-300 °C).[35] Furthermore, when exposed to H_2O at high temperatures, site relocation, dealumination and breakdown of the pore structure may occur, known as hydrothermal deactivation.[36]

Diesel contains small amounts of sulfur and SO_2 is formed during combustion. In the after-treatment system, a diesel oxidation catalyst (DOC) is commonly placed upstream of the NH_3-SCR catalyst, which may oxidize a part of SO_2 to SO_3, hence, both of these sulfur species will be present in the gas entering the catalyst. Cu-CHA is generally prone to sulfur deactivation compared to large pore size zeolite[24] and Fe-based zeolites.[37] Even small amounts of sulfur can accumulate in the zeolite and lead to substantial deactivation.[38] The exposure of the catalyst to sulfur might lead to the formation of sulfuric acid, ammonium (bi)sulfate, and Cu-sulfates.[39] A large part of the sulfur-induced deactivation can be regenerated by increasing the temperature to 500 °C, which is done periodically during operation, extending the lifetime of the catalyst. However, some of the strongly bound sulfur remains in the zeolite and is not removed during the regeneration, resulting in a loss of activity over time.[40] The poisoning mechanism with sulfur is a complex process and depends on numerous factors, such as gas composition (O_2, H_2O, NO and NH_3), and temperature. There are some promising ways to limit sulfur deactivation by, for example, constructing a core-shell structure,[41] however, these methods are in the early stage of development.

1.5 Objectives

The objective of the thesis is to investigate NH_3-SCR over a Cu-CHA zeolite with a focus on sulfur deactivation to gain a deeper mechanistic understanding.

Cu-CHA is a dynamic system, where the state of Cu changes depending on temperature and gas composition.[42] Several experimental procedures exist that quantify the different Cu sites, for instance, H_2-TPR, which is studied in **Paper 1**. In **Paper I**, density functional theory (DFT) calculations are performed to study H_2 dissociation over Cu sites, which is used to construct a mean-field model to simulate H_2-TPR profile. In addition H_2-TPR experiments are carried out to support our findings. This work will aid future interpretations of H_2-TPR profiles.

Paper II and **Paper III** focus on the sulfur poisoning. In **Paper II** a detailed reaction mechanism is proposed for the deactivation of the low-temperature NH_3-SCR by SO_2. A thermodynamic analysis is carried out to construct a phase diagram to investigate the most stable sulfur species at reaction conditions. As sulfur is proposed to limit the mobility of NH_3 solvated Cu species, constrained ab initio molecular dynamic simulation is performed to investigate the free energy barriers. In **Paper III** sulfur poisoning with both SO_2 and SO_3 at high-temperature and its effect on ammonium nitrate and N_2O formation is investigated. DFT calculations for sulfur interaction with Cu complexes are performed to facilitate the interpretation of the experimental results.

In **Paper IV**, a machine learning force-field (ML-FF) is constructed that is trained using DFT data. The ML-FF is used to investigate the mobility and pairing of $[Cu(NH_3)_2]^+$ complexes in Cu-CHA. Molecular dynamic simulations for systems with thousands of atoms for nanoseconds are performed to investigate the effect of Si/Al ratio, Cu loading, counter ion, and Al distribution. MD simulation using metadynamics is performed to investigate the diffusion between zeolite cages.

The thesis contains six chapters with the introduction being the first. In chapter two, the electronic energy obtained from both density functional theory and machine learning force-fields is discussed. Chapter three introduces methods for simulating the system at elevated pressures and temperatures, such as molecular dynamics and micro-kinetic modeling. Chapters four and five present an overview of the results obtained and chapter six is the conclusions and outlook.

2

Electronic Energy

The knowledge about the electronic energy as a function of nuclear coordinates is fundamental to the study of chemical reactions. The electronic energy can be calculated by solving the Schrödinger equation using the approximation within density functional theory. First-principle calculations are computationally expensive and an alternative approach is to parameterize the electronic energy by means of machine learning force-fields. The parameterization allows simulations of larger systems and longer simulation times. This chapter will introduce both of these methods.

2.1 The Schrödinger Equation

The time-independent Schrödinger equation is given by:

$$\hat{H}\psi = E\psi \tag{2.1}$$

$\hat{H}$ is the Hamiltonian operator, ψ is the wavefunction and E is the energy. The Hamiltonian can be written with operators for the potential and kinetic energies of the electrons and nuclei. It is convenient to write the Schrödinger equation in atomic units (au), which is defined as $m_e = e = \hbar = \frac{1}{4\pi\epsilon_0} = 1$.

$$\begin{aligned}\hat{H} = &-\sum_{A}^{nuclei} \frac{1}{2M_n}\nabla_n^2 - \sum_{i}^{elec}\frac{1}{2}\nabla_e^2 - \sum_{A}^{nuclei}\sum_{i}^{elec}\frac{Z_A}{R_A - r_i} \\ &+\sum_{i}^{elec}\sum_{j>i}^{elec}\frac{1}{r_i - r_j} + \sum_{A}^{nuclei}\sum_{B>A}^{nuclei}\frac{Z_a Z_b}{|R_A - R_B|}\end{aligned} \tag{2.2}$$

The first two terms are the kinetic energy of the nuclei and electrons, respectively. The last three terms are the Coloumb interaction between nucleus-electron, electron-electron, and nucleus-nucleus, respectively. An essential part when solving the Schrödinger equation is the Born-Oppenheimer approximation, allowing us to treat the wavefunction of the nuclei and electrons separately. This approximation is based on the fact that the nuclei have high masses compared to electrons, meaning that the nuclei can be seen as static relative to the motion of the electrons. This makes it possible to express the electronic part using nuclear coordinates.

2.2 Density Functional Theory

Using the Schrödinger equation (2.1), only one electron systems such as ${H_2}^+$ can be solved analytically. Thus, the solution needs to be approximated using numerical methods. One of the first approaches developed to solve the Schrödinger equation is the Hartree-Fock (HF) approximation.[43,44] In HF, the one-electron orbitals are arranged in a Slater determinant. The Slater determinant satisfies the requirement that the total electronic wavefunction must be asymmetric, meaning that the wavefunction must change sign when interchanging two electron coordinates. The HF energy is given by:

$$E_{HF} = \sum_{i=1}^{N_{elec}} h_i + \frac{1}{2} \sum_{i=j}^{N_{elec}} \sum_{j=1}^{N_{elec}} (J_{ij} - K_{ij}) + V_{nn} \tag{2.3}$$

h_i is the energy given by the one-electron kinetic energy operator.

$$h_i = \langle \phi_i(1)| - \frac{1}{2}\nabla_i^2 - \sum_{A}^{N_{nuclei}} \frac{Z_A}{|R_A - r_i|} |\phi_i(1)\rangle \tag{2.4}$$

J_{ij} is the Coulomb integral and K_{ij} is the exchange integral. J_{ij} and K_{ij} are given by

$$J_{ij} = \langle \phi_i(1)\phi_j(2)| \frac{1}{|r_1 - r_2|} |\phi_i(1)\phi_j(2)\rangle \tag{2.5}$$

$$K_{ij} = \langle \phi_i(1)\phi_j(2)| \frac{1}{|r_1 - r_2|} |\phi_j(1)\phi_i(2)\rangle \tag{2.6}$$

V_{nn} is the nuclear repulsion. HF does not contain the full electron correlation as the many-body wavefunction is described by a single Slater determinant. The electron-electron repulsion is instead included in an average fashion. On the other hand, HF contains the exact exchange energy, which means that any electron self-interaction is absent.

In 1964, Hohenberg and Kohn proposed two theorems that form the basis for DFT methods used today.[45] The first theorem states that the external potential V_{ext} is a unique functional of the electron density, ρ, which means that the ground state is also a unique functional of the electron density. The second theorem states that the ground state energy is a unique functional of the electron density. The clear advantage of using the electron density, ρ compared to wavefunction-based approaches is that the electron density, in principle, has the same number of variables independent of the size of the system. However, the functional connecting the energy and electron density is unknown.

Attempts at solving the ground state energy only from the electron density results in poor accuracy, with one reason being the difficulty in describing the kinetic energy. A solution is the introduction of Kohn-Sham orbitals,[46] used in modern DFT calculations. Here, the DFT energy can be written as

$$E_{DFT}(\rho) = T_S(\rho) + E_{ne}(\rho) + J(\rho) + E_{xc}(\rho) \tag{2.7}$$

$T_S(\rho)$ is the kinetic energy expressed by single-electron orbitals for non-interaction electrons, where the wavefunction is constructed from a single Slater determinant similar to HF.

$$T_S(\rho) = \sum_{i=1}^{N_{elec}} \langle \phi_i| - \frac{1}{2}\nabla^2 |\phi_i\rangle \tag{2.8}$$

$E_{ne}(\rho)$ is the interaction between the nucleus and electrons, $J(\rho)$ is the electron-electron repulsion. For the first three terms, there are exact solutions available. However, for the exchange-correlation energy $E_{xc}(\rho)$, an approximation is needed.

2.2.1 Exchange Correlation Functionals

$E_{xc}(\rho)$ can be given as the sum of the exchange energy $E_x(\rho)$ and correlation energy $E_c(\rho)$. The different ways of approximating $E_{xc}(\rho)$ give rise to the many methods within DFT. A simple approximation is the local density approximation (LDA)[45] where the density is treated locally as a uniform electron gas. Here the exchange energy is given as

$$E_x^{LDA}(\rho) = -\frac{3}{4}\left(\frac{3}{\pi}\right)^{1/3} \int \rho^{4/3}(r)dr \tag{2.9}$$

The correlation energy, E_c^{LDA} can be calculated with high accuracy based on quantum Monte Carlo simulations.[47] The approximation of a uniform electron gas fails in cases where the electron density does not vary slowly, for example, in the case of molecular systems.

Improvements to LDA are possible by making the exchange-correlation depend on not only the electron density but also on the first derivate. One of these methods is known as generalized gradient approximation (GGA)[48] and the exchange energy can be written as

$$E_x^{GGA}(\rho, x) = \int \rho^{4/3} F(x) dr \tag{2.10}$$

$F(x)$ is an enhancement factor that depends on the method used. x is the dimensionless density gradient. One well-known approximation within the GGA class is Perdew-Burke-Ernzerhof (PBE),[49] which is used in this thesis. Here, the enhancement factor is

$$F(x) = 1 + \kappa - \frac{\kappa}{1 + \mu x^2/\kappa} \tag{2.11}$$

κ and μ are constants. The correlation energy, E_c^{GGA} is expressed as the local correlation together with an additive term. A way to make the approximation better is to let the exchange-correlation energy depend on higher-order derivatives of the electron density, which includes the kinetic energy density and is called meta-GGA methods.[50]

Common for the LDA and GGA methods, is that they tend to over delocalise the electrons because the exchange-correlation term E_{xc}, cannot properly remove the self-interaction from the electron-electron interaction. This is especially important for the description of strongly correlated d- or f-electrons, which typically is the case for transition-metal oxides. In HF, this electron self-interaction is removed by the HF exchange. In hybrid methods, the problem is reduced by adding a fraction of the HF exchange to the exchange-correlation. One example of a hybrid method is B3LYP.[51,52]

$$E_{xc}^{B3LYP} = (1-a)E_x^{LSDA} + aH_x^{HF} + b\Delta E_x^{B88} + (1-c)E_c^{LSDA} + cE_c^{LYP} \tag{2.12}$$

Two different exchange energies are included, which is the exchange from HF, E_x^{HF} and B88, E_x^{B88}. The correlation part is the LYP functional E_c^{LYP}. The amount of exchange included is determined by the parameters a, b, and c, which are fitted to experimental data. Hybrid methods generally give more accurate results than GGA methods, however, there is an increasing computational cost associated with the calculation of HF exchange.

Another way to reduce the issue with the self-interaction is augmenting DFT with a Hubbard U term.[53] Here, the strong on-site Columb interactions of the localized electrons are treated with an additional term, which stabilizes the localized orbitals with respect to delocalization. The choice of the U parameter is important and is method and material dependent. Typically different values of U are tested and compared with experiments or computational results. The U value can also be determined from first-principles[54].

A drawback of standard density functional theory is that it does not contain dispersion forces and therefore cannot capture the attractive $1/R^6$ long-distance behavior. A solution is to add an empirical pairwise correction as suggested by Grimme[55] that accounts for the dispersion forces.

$$\Delta E_{disp} = -\sum_{n=6(8,10)} s_n \sum_{AB}^{atom} \frac{C_n^{AB}}{R_{AB}^n} f_{damp}(R_{AB}) \tag{2.13}$$

s_n is a scaling factors that depends on the functional applied, C_n^{AB} is a dispersion coefficient, for atom pair AB and R_{AB}^n is the distance between A and B for the n$^{\text{th}}$ order(n=6(8,10)). $f_{damp}(R_{AB})$ is the damping factor. Early models[50] included only the 6$^{\text{th}}$ order term, but can be refined by including higher orders corrections. This correction is referred to as DFT-D methods, where the DFT-D3 approach is used in this work.

2.2.2 Basis Sets and Pseudopotentials

When solving HF or DFT, they both require a basis set to represent the orbitals. This can either be done with a Slater and Gaussian-type of orbitals centered at the atoms or in the form of plane waves. In this work, plane waves are used as they are the preferred choice for periodic systems, as they fulfill Bloch's theorem. Bloch's theorem states that the plane wave functions, at the same position in two different cells can be related by the lattice vector t.

$$\phi(r+t) = e^{ik\cdot r}\phi(r) \tag{2.14}$$

Plane waves are good at describing delocalized slowly varying electron densities, such as valence and conduction bands as the potential is rather smooth. However, this is not the case for core electrons that are localized with sharp peaks and many oscillations that would require many plane waves to describe. A solution to this problem is to treat the core electrons with an effective potential and only treat the valence electrons explicitly, which at the same time decreases the computational cost. This is possible since the core electrons are not involved in the formation and breaking of chemical bonds. These methods are known as pseudopotential methods and the Projector Augmented Wave (PAW)[56] proposed by Bloch is used in this thesis.

2.2.3 Bader Charge Analysis

Analysis of atomic charges is useful as it allows for studies of, for example, the oxidation state of Cu ions. The method of Bader charge analysis is used in this thesis.[57,58] In Bader charge analysis, the charge density is partitioned into Bader volumes corresponding to each atom, which are separated by zero flux surfaces, where the charge density is a minimum perpendicular to the surface. Each Bader volume contains a single electron density maximum. Henkelman and co, developed a method to partition the charge density into Bader volumes.[57,58] The method is grid-based and the partition algorithm follows the steepest ascent path along the charge density gradient until the maximum electron density is found. The total charge is then calculated by integrating over each Bader volume.

2.3 Parameterization of Energy

DFT is a powerful tool for calculating the electronic energy from the Schrödinger equation. However, DFT calculations have a high computational cost, which puts a limitation on what problems can be studied. Instead of solving the DFT-equations, the electronic energy can be calculated by parameterizing it as a function of nuclear coordinates, known as force-fields (FF).

2.3.1 Force-Field

The force-field energy can generally be written as different bonded and non-bonded terms contributing to the energy.[59]

$$E^{FF} = E_{str} + E_{bend} + E_{tors} + E_{vdw} + E_{el} + E_{cross} \tag{2.15}$$

E_{str} is the energy contribution from stretching of the bonds, E_{bend} describes the energy as a function of bending an angle between three atoms, E_{tors} is the torsion between four atoms. E_{vdw} and E_{el} describe the van der Waals and electrostatic contributions to the energy. Finally, E_{cross} represents the coupling between the different terms. The bonding terms ($E_{str} + E_{bend} + E_{tors}$) can be described by simple functions of distance, angle, and torsion, respectively. For the non-bonding terms, the van der Waals forces, E_{vdw} can be modeled using a Lennard-Jones potential while the electrostatic energy E_{el} can be modeled using a Coulomb law assuming point charge, however, higher-order forms may be included. The parameters are typically fitted to experimental or higher-level ab initio data. By parameterizing the electronic energy, and bypassing the DFT equations, it becomes possible to study systems with thousands of atoms. However, traditional FF, can be time-consuming to construct and require a detailed knowledge of how to model the system.[60] Conventional force-fields such as AMBER[61] and UFF,[62] assume that the bonds between the atoms are predefined, and that bond formation and breaking do not occur, which limits its application.[63] More advanced bond-order force-fields like ReaxFF,[64] can model reaction, as the bonds are determined during the simulation,[65] however, this adds more complexity to the force-field.

2.3.2 Machine Learning Force-Fields

The main problem with FF is the poor accuracy compared to, for example, DFT calculations. A promising way to combine the accuracy of DFT with the low computational cost of FF is by using machine learning (ML-FFs).[63] Here, the energy and forces are predicted through the use of machine learning and do not consist of analytical expressions as is the case for FF. ML-FF is an emerging field whereby training a force-fields on for example DFT data, an accuracy close to DFT can be achieved with a computational cost close to that of a traditional force-field. In addition, the process of constructing a force-field is simplified by using machine learning.

In ML-FF, the total energy is a sum of the energies of the individual atoms.

$$E_{tot}^{ML-FF} = \sum_i E_i \tag{2.16}$$

The energy of each atom, E_i is determined by the local atomic environment, determined by a radius cut-off value r_{cut}, illustrated for atom A in Figure 2.1(a). To describe the local atomic environment, several descriptors can be implemented. Two simple descriptors are the distance r_{A-C} between atom A and C together with the angle θ_{B-A-C} between atom B, A and C illustrated in Figure 2.1. Here, the energy of atom A depends on the atoms within the cut-off value, which are atoms B and C. However, atom D is outside the cut-off values, and thus the energy of atoms A and D does not depend explicitly on each other. The assumption of chemical locality reduces the computational cost as the interaction between all atoms does not have to be calculated. Furthermore, it makes it possible to extrapolate the ML-FF to larger systems after training. However, the drawback is the inability to describe long-range interactions, which can be important for, especially, charged systems.[66]

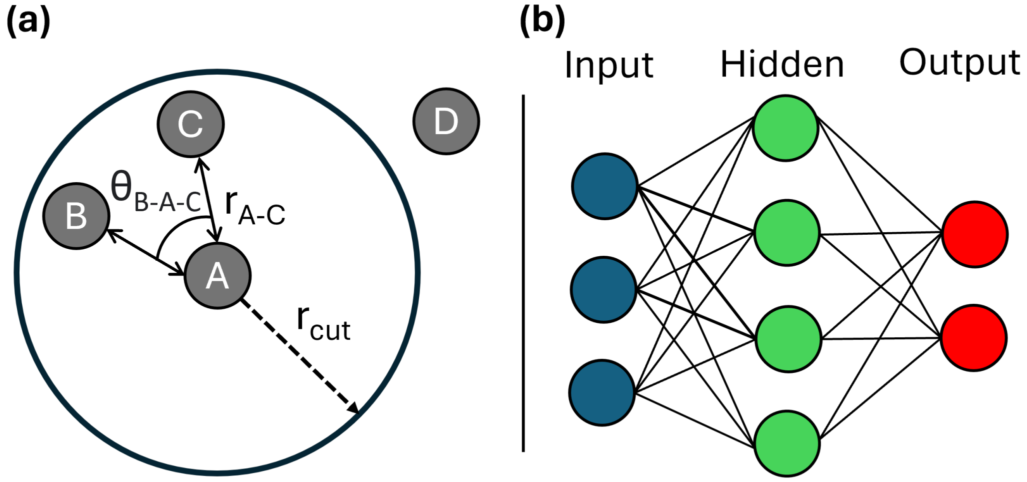

Figure 2.1: (a): The description of local atomic environment for atom A (b): A simple neural network showing three different layers, being the input layer, hidden layer and output layer.

2.3.3 Long-range Interactions

A way to add long-range interaction to an ML-FF is by the use of atom-centered point charges. The ML-FF energy can in this way be augmented with the electrostatic energy. Here, a recently developed method by Zhang et al[67] implemented in the Deep MD kit code[68] is used. The code was originally used with maximally localized Wannier functions. Here, however, atom-centered point charges are used instead. The energy is

$$E_{tot}^{ML-FF} = E_{sr} + E_{G_t} \tag{2.17}$$

E_{sr} is the predicted energy from standard ML-FF using a radius cut-off value. The introduced E_{G_t} term is the Gaussian electrostatic energy. Note that the Gaussian electrostatic energy E_{G_t} is subtracted from E_{sr} to avoid double counting. E_{G_t} is calculated in the Fourier space as

$$E_{G_t} = \frac{1}{2\pi V} \sum_{m \neq 0, |m| \leq L} \frac{\exp(-\pi^2 m^2/\beta^2)}{m^2} S(m)^2 \tag{2.18}$$

V is volume of the unit cell, L is the Fourier space cutoff and β is the spread parameter. S(m) is the structure factor given by

$$S(m) = \sum_i q_i e^{-2\pi i m R_i} \tag{2.19}$$

q_i is the charge density of charge i, and R_i is the charged site. The particle-particle-particle-mesh (PPPM) algorithm is used to calculate the electrostatic energy. Note that it is not necessarily all atoms that are assigned a point charge. The incorporation of the Gaussian electrostatic energy increases the computational cost by approximately a factor of 5 but is still superior in speed when compared to DFT calculations.[67]

2.3.4 Neural Network

Having introduced the descriptors in equation 2.16, the next step is to go from the descriptors to electronic energies and forces by the use of machine learning. Two commonly used algorithms for ML-FF are the kernel method and the neural network, which is used in this thesis.[69] The neural network is inspired by the neurons in the brain, hence, the neural network is sometimes referred to as biological neural networks. A simple neural network is illustrated in Figure 2.1b, with input, hidden, and output as the layers. In reality, a neural network may have hundreds of neurons with several hidden layers depending on the complexity of the problem studied. The objective of the hidden layer is to transform the input (descriptors), into output (energy and forces). A single hidden layer can be written as

$$f(x) = \sum_{n=0}^{N} c_n \sigma(w_n x + b_n) \tag{2.20}$$

$f(x)$ corresponds to the output and x is the input. N is the number of neurons and σ is the neuron activation function. c_n, w_n and b_n are parameters fitted to a given set of training data.

The parameters are fitted by constructing a loss function.[68]

$$L(p_\epsilon, p_f, p_\xi) = p_\epsilon \Delta\epsilon^2 + \frac{p_f}{3N}\sum_i |\Delta F_i|^2 + \frac{p_\xi}{9}||\Delta\xi||^2 \tag{2.21}$$

Δ is the difference between the force-field prediction and the training data, N is the number of atoms, ϵ is the energy per atom, F_i is the force on atom i, and ξ is the viral tensor (if included). p_ϵ, p_f and p_ξ are adjustable parameters, where $p_\in$ and p_f are increasing, and p_ξ decreasing during training. The training is a minimization problem of the loss function by tuning the parameters in the hidden layer(s). The training data used in this thesis is DFT data from structures extracted during molecular dynamic simulation trajectories.

3

Towards Elevated Pressure and Temperature

Structures and transition states, which are needed to investigate chemical reactions can be identified by performing optimization procedures. However, the calculated electronic energy corresponds to zero kelvin and zero pressure, which does not represent experimental conditions. With statistical mechanics and thermodynamics, it is possible to add temperature and pressure effects to the electronic energies. An alternative approach is to solve Newton's equations of motion and simulate the system at finite temperatures and/or pressures via molecular dynamics (MD). Combined with ML-FF, it is possible to simulate several nanoseconds. Micro-kinetic modelling can be used to study the time evolution of chemical reactions over extended times. In a first principle-based micro-kinetic model, a set of differential equations is solved using rate constants derived from first-principle calculations. This chapter will discuss the process of adding the effects of temperature and pressure to the electronic energies calculated in the previous chapter, and methods to model reaction kinetics.

3.1 Optimization

The search for a stable structure is a multidimensional optimization problem, where the nuclear coordinates are changed to minimize the energy of the system. The objective is to find a local minimum on the potential energy surface, hence, the gradient in all directions should be zero. Using first-principle calculations or ML-FF, it is possible to determine the energies and forces of the potential energy landscape, that can be used by different algorithms to obtain a minimum. A simple approach is to calculate the gradient and then take a step in the opposite direction, known as the steepest descent (MD) method.[50] Going in the opposite direction of the gradients, ensures that the energy will decrease, thus, it is guaranteed that a minimum will be found. However, SD tends to oscillate around the minimum and the convergence is slow.[50] A way to improve on the SD method, is to consider both the gradient and the gradient from the previous step. By doing so, the step is not taken against the gradient but along a line conjugate to the previous step. This ensures faster convergence than the SD method. This method is called conjugate gradient and is the method used in this thesis. Another method is the Newton-Raphson method, which uses the second-order derivatives. Note that these methods only ensure that the structure converges to a local minimum, thus, it might not correspond to a stable structure. This is especially challenging for species in Cu-CHA as the potential energy landscape is flat. Here, this issue has been tackled by using ab initio molecular dynamics (AIMD) to sample the potential energy landscape.

3.2 Transition State Search

Chemical reactions typically involve some kind of energy barrier that has to be passed to form the final products. The molecules follow the minimum energy path between the two states with the highest point connecting them corresponding to the transition state, which is a first-order saddle point. For periodic systems, multi-structure interpolation methods such as the climbing image nudge elastic band (CI-NEB) are generally used to identify the transition states.[50] In NEB, a series of structures, called images are interpolated between the initial and final state, which must be known. A spring is added that evenly distributes the images, along the reaction coordinate, mimicking an elastic band, hence the name. The images are optimized based on the perpendicular component of the true force, ensuring that the spring force does not interfere with the convergence of the images to the minimum energy path.[70] To find the transition state, the spring of the image with the highest energy is turned off, so the image experiences the true forces.[71] This image is, thereafter, converged to a first-order saddle point.

3.3 Vibrations

At zero Kelvin, the molecules still vibrate and typically a correction to the electronic energy is added, giving the zero point energy (ZPE). The vibrations can be approximated as that of a harmonic oscillator. The vibrational frequencies can with this approximation be derived by a Taylor expansion involving the energy and nuclear coordinates. For a diatomic molecule, the only nuclear coordinate to consider is the bond length and the Taylor series becomes the following.[50]

$$E(R) = E(R_0) + \frac{dE}{dR}(R-R_0) + \frac{1}{2}\frac{d^2E}{dR^2}(R-R_0) + \frac{1}{6}\frac{d^3E}{dR^3}(R-R_0)^3 + ... \tag{3.1}$$

The first term is the zero point of the energy, the second term vanishes since the structure vibrates around a minimum where the first derivate with respect to the nuclear coordinates is zero. The energy can, thus, be approximated as the lowest non-zero term, which is the second-order derivative.

$$E(R-R_0) \approx \frac{1}{2}\frac{d^2E}{dR^2}(R-R_0) = \frac{1}{2}k(R-R_0) \tag{3.2}$$

The second derivative is defined as the force constant k, which can be used to estimate the vibrational frequency v.

$$v = \frac{1}{2\pi}\sqrt{\frac{k}{\mu}} \tag{3.3}$$

μ is the reduced mass that for a diatomic molecule is $m_1m_2/(m_1+m_2)$.

3.4 Statistical Mechanics

The structure and transition states discussed so far, correspond to structures at zero Kelvin at zero pressure. Statistical mechanics provide the connection between the properties of a single molecule and an ensemble of molecules at elevated temperatures and pressures. Essential for the connection is the partition function Q as several thermodynamic properties can be derived from the partition function[72] such as enthalpy H, entropy S, Helmholtz free energy F, and Gibbs free energy G.

$$H = U + PV = k_B T^2 \left(\frac{\partial \ln Q}{\partial T}\right)_V + k_B T V \left(\frac{\partial \ln Q}{\partial V}\right)_T \tag{3.4}$$

$$S = \frac{U - F}{T} = k_B T \left(\frac{\partial \ln Q}{\partial T}\right)_V + k_B \ln Q \tag{3.5}$$

$$F = -k_B T \ln Q \tag{3.6}$$

$$G = H - TS = k_B T V \left(\frac{\partial \ln Q}{\partial V}\right)_T - k_B T \ln Q \tag{3.7}$$

For a system consisting of N non-interaction, indistinguishable particles, the partition function Q is defined as $Q = \frac{1}{N!} q^N$. q is the partition function for a single molecule, which is given by the sum of all possible quantum energy states.

$$q = \sum_i^{\infty} e^{-\epsilon_i / k_B T} \tag{3.8}$$

The total partition function can be written as a product of terms involving the electronic, translation, rotation, and vibration degree of freedoms.

$$q_{tot} = q_{trans} q_{rot} q_{vib} q_{elec} \tag{3.9}$$

The translation has three degrees of freedom, and the partition function depends on the volume V and the mass m.

$$q_{trans} = \left(\frac{2\pi m k_B T}{h^2}\right)^{3/2} V \tag{3.10}$$

Using the rigid-rotor approximation the rotational partition function for a polyatomic molecule can be calculated using the principal axes of inertia I_x and a symmetry factor σ.

$$q_{rot} = \frac{\sqrt{\pi}}{\sigma} \left(\frac{8\pi^2 k_B T}{h^2}\right)^{3/2} \sqrt{I_1 I_2 I_3} \tag{3.11}$$

The vibrational partition function can be written as a product involving the vibrational frequencies v_i. The number of vibrations is $3N - 6$ for a non-linear molecule, with N being the number of atoms.

$$q_{vib} = \prod_{i=1}^{3N-6} \frac{e^{-h v_i / 2 k_B T}}{1 - e^{-h v_i / k_B T}} \tag{3.12}$$

The partition function for the electronic degree of freedom is a sum of all quantum states. However, since the energy difference between the ground and exited states typically is large compared to k_BT, only the ground state becomes important. This means that the partition function can be approximated by only the ground state.

$$q_{elec} = \sum_{i=0}^{\infty} g_i e^{-\epsilon_i/k_BT} \approx g_0 e^{-\epsilon_0/k_BT} \tag{3.13}$$

Defining the ground state energy as the zero point energy, the partition function becomes equal to the degeneracy g_i.

The calculation of the entropy from partition functions is not straightforward. For surface-bound atoms, the contribution from translation and rotation degree of freedom is typically assumed to be small since the movement is restricted. In this case, the entropy is calculated from the vibrational frequencies. However, for zeolites, this becomes challenging since the species may contain a significant amount of translation and rotational entropy.[73] An alternative way to calculate the free energy for such systems is by molecular dynamics.

3.5 Molecular Dynamics

In molecular dynamics (MD), the motion of the atoms is simulated at elevated temperatures and pressures. The motion of the nuclei is heavy enough to be approximated as classic particles. The motion can in this case be described by Newton's second law.

$$F = ma \tag{3.14}$$

F is the force, m is mass and a is acceleration. Newton's equations of motion for a set of atoms can be solved numerically using the Verlet algorithm.[74] Here r_i is the initial position and r_{i+1} is the new position.

$$r_{i+1} = (2r_i - r_{i-1}) + \frac{F_i}{m_i}\Delta t^2 \tag{3.15}$$

Δt is the timestep. If the force is evaluated using first-principle calculations, it is called ab initio molecular dynamics (AIMD). The force can also be estimated using ML-FF from which simulation times in the range of nanoseconds can be achieved. The choice of the timestep Δt, depends on the application. A large timestep allows for long simulation times, as the forces have to be evaluated less frequently. However, a too large timestep can lead to inaccuracies in the simulation as rapid changes may not be captured. The choice of timestep typically depends on the lightest atom included in the simulation, as they vibrate faster, a smaller timestep is therefore needed for systems containing hydrogen atoms. If the vibration of the hydrogen atoms is not of interest, they may be slowed down by increasing the mass or simply freezing the bond length allowing a higher time step.[50]

To mimic experimental conditions in the MD simulations, different thermodynamic ensembles exist that have different degrees of isolation from the surroundings. The most simple one is the microcanonical ensemble (NVE), where the system has a constant number of atoms, volume, and energy. Typically an experiment can exchange heat with the surroundings, and in this case, an NVT ensemble is a more suitable choice, where instead of the energy, the temperature is kept constant. A third option typically encountered in MD simulation is the NPT ensemble where the pressure is kept constant, hence the volume is allowed to change. In reality, the temperature is not fixed at all times but fluctuates around the target temperature, controlled by a thermostat. A popular thermostat is the Nosé-hoover thermostat,[75,76] which is used in this thesis. Here a heat bath is coupled to the physical system via the Lagrangian.

$$L = \sum_{i=1}^{N} \frac{m_i}{2} s^2 \left(\frac{dr_i}{dt}\right)^2 - U(r) + \frac{Q}{2}\left(\frac{s}{dt}\right)^2 - gk_BT \ln s \tag{3.16}$$

The first two terms correspond to the kinetic and potential energy of the system, respectively. The variable s introduces an extra degree of freedom into the system, Q is the effective mass of s and g is the number of degrees of freedom of the system ($g = 3N$, where N is the number of atoms).

In MD simulations, the atoms tend to stay around their minimum energy and rare events may require a very long simulation time to be observed. The use of ML-FF to run molecular dynamic simulations does improve this, but the problem still exists. A way to estimate the free energy barrier of rare events is to apply a bias that forces the transition to happen more frequently, known as enhanced sampling techniques.

3.6 Enhanced Sampling Technique

Common for all enhanced sampling techniques is the need to define a collective variable (CV) that represents the reaction path for which the free energy is estimated. A simple CV could be a bond length, angle, torsion, or combinations of them. More advanced CV's include the Path Collective Variables,[77] where the CV is adapted to the lowest energy path connecting two structures. Typically only one CV is investigated per simulation, however, some methods allow the sampling of a multi-dimensional reaction landscape. Common methods used to sample the free energy barriers are the slow growth[78] and metadynamics,[79] both of which are using this thesis. In the slow-growth method, the CV is linearly changing from an initial value to a final value thereby, estimating the electronic energy along the reaction path. Using the blue moon approach, it is possible to estimate the free energy profiles.[80] Here, the free energy can be obtained by integrating the free energy gradients along the CV, ξ.

$$\Delta A_{1\to 2} = \int_{\xi(1)}^{\xi(2)} \left(\frac{\partial A}{\partial \xi}\right)_{\xi^*} d\xi \tag{3.17}$$

3.6.1 Metadynamics

The idea behind metadynamics is that the potential energy wells are filled with Gaussians making it possible to sample the rare events more frequently. In metadynamics, Gaussian functions are added during the simulation[81], where the bias V can be defined as.

$$V(s,t) = \sum_{kr<t} W(k\tau) \exp\left(-\sum_{i=1}^{d} \frac{(s_i - s_i^{(0)}(k\tau))^2}{2\sigma_i}\right) \tag{3.18}$$

The bias $V(s,t)$, is added to the potential energy landscape, which can force the molecule through transitions that otherwise would not happen during the timescale of the simulation. W and σ are the width and height of the Gaussian function, s and s^0 are the values of the CV and the CV where the Gaussian function is added respectively. A popular version of the method is well-tempered metadynamics[79], where the height of the Gaussian W decreases over time, resulting in a more smooth convergence. In the long time limit, the bias potential should converge to the negative Helmholtz free energy F, with a constant C.

$$V(s, t \to \infty) = -F + C \tag{3.19}$$

The free energy can be estimated directly from the added Gaussian as shown in (3.19). In cases where one is interested in studying other CVs than what has been used in the simulations, it is possible to do so by reweighting the bias.[82] Figure 3.1(a) shows the free energy estimates at different times. As the simulation time increases the free energy profiles at different times should converge. The exploring of the CV during the simulation is illustrated in Figure 3.1(b). The system oscillates around the reaction path, slowly refining the free energy profiles. As the simulation above is with well well-tempered metadynamics, the height of the Gaussian function as a function of simulation decreases, see Figure 3.1c. The idea behind well-tempered metadynamics is that the first Gaussian functions are used to fill up the potential energy wells and a high Gaussian height makes the sampling faster. When the potential energy wells are filled, smaller Gaussian functions are used to refine the free energy profile which should lead to a smooth convergence in the long time limit.[79]

The use of MD simulations combined with ML-FF makes it possible to simulate for a few nanoseconds, however, typical experiments are run for minutes to several hours. To overcome this micro-kinetic modeling can be used, where a set of coupled differential equations is solved.

3.7 Micro-Kinetic Modeling

In micro-kinetic modeling, a reaction path with elementary steps is first constructed. This should include the formation of desired products, but may also contain side reactions. The rate constant of the reaction has to be calculated, which could be done using DFT calculations. In transition state theory (TST), the reaction rate is given by.[83]

$$k = \frac{k_B T}{h} e^{-\Delta G^\ddagger / k_B T} \tag{3.20}$$

$\Delta G^\ddagger$ is the free Gibbs energy difference between the transition state and initial state. The change in Gibbs free energy can be calculated from the enthalpy and entropy.

$$\Delta G = \Delta H - T\Delta S \tag{3.21}$$

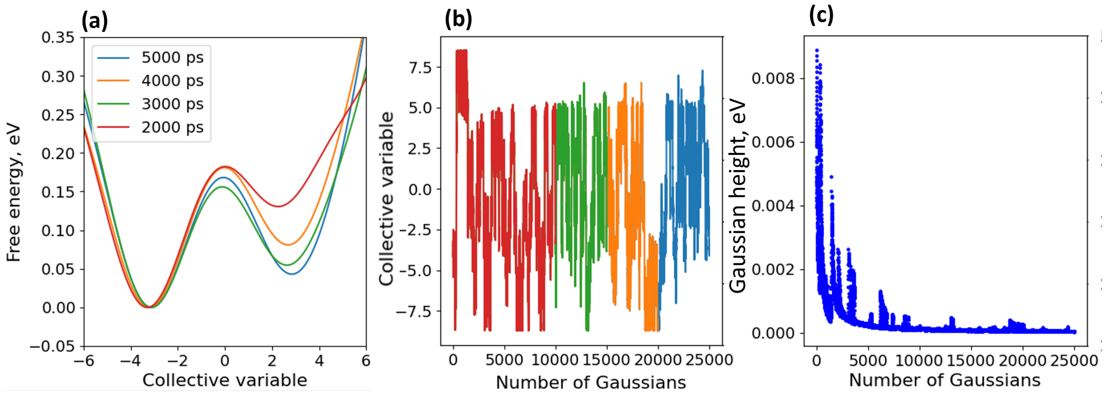

Figure 3.1: Well-tempered metadynamics simulations. (a): Estimated free energy profiles calculated at different simulation times. (b): Value of the CV for every Gaussian function deposited during the simulation. (c): Height of the Gaussian during the simulation.

The enthalpy can be approximated as the zero point corrected electronic energy E by neglecting the pV-dependence. The entropy can be calculated using partition functions introduced earlier. Note that the reaction coordinate should be excluded from the partition function of the transition state. Combining equation 3.20 and 3.21, the rate constant become.

$$k = \frac{k_B T}{h} e^{-\Delta H^{\ddagger}/k_B T} e^{\Delta S^{\ddagger}/k_B} \approx \frac{k_B T}{h} e^{-\Delta E^{\ddagger}/k_B T} e^{\Delta S^{\ddagger}/k_B} \tag{3.22}$$

For adsorption reactions, the rate constant is calculated using collision theory.

$$k = \frac{pA}{\sqrt{2\pi m k_B T}} e^{-E^{\ddagger}/k_B T} \tag{3.23}$$

A is the area of the active site, p is the partial pressure, and m is the mass. To ensure thermodynamic consistency, the reverse rate constant is calculated from the equilibrium constant

$$K = \frac{k_f}{k_r} = e^{-\Delta G/k_B T} \tag{3.24}$$

k_f and k_r are the forward and reverse rate constant, respectively, and ΔG is the free Gibbs change between the final and initial state.

To simulate the kinetic of the system, a set of coupled differential equations are solved numerically.

$$\frac{d\theta_i}{dt} = \sum_j v_{ij} r_j \tag{3.25}$$

θ_i is the coverage of species i, v_{ij} is the stoichiometric coefficient for reaction j, and species i. r_j is the rate of reaction j and is given by the rate constant and coverage.

$$r_j = k_j^f \prod_f \theta_f - k_j^r \prod_b \theta_b \tag{3.26}$$

Temperature-programmed reduction (TPR) is an experimental analysis where the sample is exposed to a reducing gas such as H_2, during a temperature ramp. From this valuable information, such as the reduction temperature of active sites can be obtained. Micro-kinetic modeling can be used to simulate TPR experiments by introducing a time-dependent temperature.

$$T = T_0 + \beta t \tag{3.27}$$

T_0 is the starting temperature, β is the heating rate and t is the time.

4

Sulfur Poisoning during NH_3-SCR

Cu-ions in Cu-CHA are dynamic in the sense that they can exist in different oxidation states (Cu^+ and Cu^{2+}) and be solvated by different ligands (H_2O, NH_3). Thus, the state of the Cu-ions depends sensitively on the temperature and feed-gas.[42] The different Cu states have different properties and, therefore, different reactivity towards sulfur species. It is, therefore, important to obtain information on which Cu species that are present in the sample. One well-known method for quantifying Cu species in Cu-CHA is temperature programmed reduction (H_2-TPR), which is studied in **Paper I**. By comparing experimental and computed TPR profiles, it is possible to make conclusions on the dominant Cu-species in Cu-CHA.

As discussed in the Introduction, the catalyst is exposed to small amounts of SO_2 and SO_3 that reduce the activity. One way to formulate strategies to mitigate sulfur poisoning is to understand the mechanisms of poisoning. The sulfur poisoning is studied for low-temperature in **Paper II** and high-temperature in **Paper III**, using DFT calculations.

4.1 State of Cu during Operating Conditions

Two Cu species, commonly discussed in the literature are Z_2Cu and ZCuOH.[42] Here, Z represents a one-Al environment and Z_2 a two-Al environment. The two Cu sites are usually attributed to H_2 consumption at 210 °C for ZCuOH and both 320 and 480 °C for Z_2Cu. However, the interpretation is not fully settled.[84–90] The H_2-TPR profiles may have different shapes and peaks depending on the pre-treatment and composition, making the interpretation complex. During NH_3-SCR conditions, NH_3 can adsorb onto the Cu ions and form mobile $[Cu(NH_3)_2]^+$ complexes that are not bound to the framework.[30,31,91] If two $[Cu(NH_3)_2]^+$ complexes are in the same cage, they can adsorb O_2, forming a peroxo complex $[Cu_2(NH_3)_4O_2]^{2+}$, which is an important intermediate in the NH_3-SCR reaction.[29,31] At higher temperature, NH_3 may desorb forming framework-bound Cu species. Framework bound Cu species beside Z_2Cu and ZCuOH, are $Z_2CuOOCu$, $Z_2CuHOOHCu$ and Z_2CuOCu.[92–94] While ZCuOH and Z_2Cu have been studied extensively for H_2-TPR in the literature, there is a limited understanding at which temperatures the alternative Cu sites consume H_2.

In **Paper I**, we constructed a microkinetic model to simulate H_2-TPR profiles to aid in the interpretation of experiments. The rate constants are calculated using

DFT and the simulated H_2-TPR profile is shown in Figure 4.1(a) with the Cu sites shown in Figure 4.1(b). Cu in oxidation state +1 is also considered, however, no energetical favored pathway was found for the adsorption of H_2. Cu in oxidation +1 is commonly assigned to TPR-signatures at temperatures above 800 °C where the destruction of the framework may occur, which is not taken into account in our calculations.[88] Our simulated H_2-TPR profiles predict that ZCuOH reduces at 150 °C and Z_2Cu at 420 °C, which is consistent with reports in the literature. However, it is also observed that the measured H_2-TPR profiles potentially would be assigned to other Cu sites such as Z_2CuOCu $Z_2CuHOOHCu$ or $Z_2CuOOCu$, as they adsorb H_2 in similar temperature ranges. One notable finding is that only two proximate Z_2Cu sites can be reduced with H_2, thus, a single isolated Z_2Cu site should not be reduced. This suggests that the Al distribution may play an important role in the reduction temperatures.

To further validate our findings, H_2-TPR experiments are performed where the sample were pretreated to contain dominant Cu sites. The experiments match our simulated profiles. This study shows that only considering ZCuOH and Z_2Cu in H_2-TPR profiles may not capture the full picture.

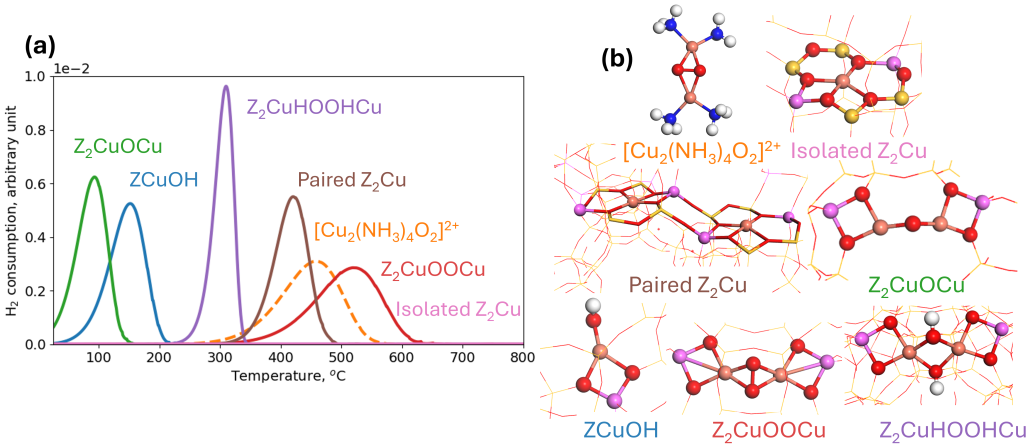

Figure 4.1: (a): Simulated H_2-TPR profile. (b): Cu species considered in the simulation.

4.2 Sulfur Poisoning

For Cu-CHA samples with low Cu loading, the NH_3-SCR activity as a function of temperature typically shows two maxima referred to as the seagull shape.[95] This is attributed to two different reaction mechanisms, at low and high temperatures. This is related to the different states of Cu complexes present in the two different temperature regimes. The reaction proceeds over $[Cu(NH_3)_2]^+$ species at low temperatures, whereas framework bound species are active sites at high temperatures.

A major challenge with the use of Cu-CHA is the sensitivity to sulfur species. The current understanding of the interaction of SO_x (x=2 and 3) species with Cu-CHA on the atomic level is limited. The studies until now have mostly been focused on ZCuOH and Z_2Cu,[86] which are active at high temperatures. Since SO_2 does not adsorb in Cu-free chabazite (H-CHA)[86], the speciation of the Cu ions is likely to influence the sulfur deactivation. SO_2 temperature-programmed desorption (SO_2-TPD) is a common procedure to quantify the sulfur derived species formed. The desorption of SO_2 at 420 °C is commonly assigned to the decomposition of $SO_4(NH_4)_2$ or $HSO_4(NH_4)$, and the two high-temperature peaks at 540 and 720 °C are assigned to sulfur bonded to Cu and Al.[96,97] Since SO_2 is released at 420 °C, periodic heating up to $\approx$ 500 °C of the catalyst is done to remove part of the sulfur species and thereby regaining some of the lost activity. The deactivation that can be recovered by the regeneration procedure is denoted reversible deactivation, while the sulfur species that are still present after regeneration are denoted irreversible deactivation.

4.2.1 Low-temperature Deactivtion

In **Paper II**, we investigated the reaction of SO_2 with Cu complexes present during low-temperature NH_3-SCR, such as $[Cu(NH_3)_2]^+$ and $[Cu_2(NH_3)_4O_2]^{2+}$. SO_2 is found not to react with $[Cu(NH_3)_2]^+$ but with $[Cu_2(NH_3)_4O_2]^{2+}$ from which a detailed reaction mechanism is proposed and illustrated in Figure 4.2. The $[Cu_2(NH_3)_4O_2]^{2+}$ complex adsorbs SO_2 from structure I to II, leading to a stable Cu sulfate structure $[Cu_2(NH_3)_4SO_4]^{2+}$ (Structure III). NO and NH_3 can couple with over the complex, forming H_2NNO that can decompose over a Brønsted site into N_2 and H_2O. In addition to N_2 and H_2O, H_2SO_4 is formed. The reaction can proceed via two routes, depending on whether it involves structures that are mobile (roman numbers) or bound to the framework (letters). Since H_2SO_4 is a bulky molecule, it can not exit the chabazite cage due to a high diffusion barrier through the eight-membered ring and may accumulate leading to a loss in activity. As NH_3 is present, H_2SO_4 can exchange proton forming $SO_4(NH_4)_2$ and $HSO_4(NH_4)$ and ab into thermodynamic analysis suggests that $HSO_4(NH_4)$ is the stable species at typical reaction conditions.

To investigate how the accumulation of $HSO_4(NH_4)$ affects the NH_3-SCR activity, constrained AIMD simulation was performed and the results are shown in Figure 4.3. The AIMD simulations was done to investigate the stability of paired $[Cu(NH_3)]^+$ complexes, which is necessary for the adsorption of O_2. If two ammonium bisulfate are present (red line), the stability of paired $[Cu(NH_3)_2]^+$ complexes is decreased, thus deactivating the catalyst. This finding implies that the sulfur deactivation at low temperatures is of physical origin.

4.2.2 High-temperature Deactivation

At higher temperatures, the $[Cu(NH_3)_2]^+$ complexes decomposes and Cu binds to the framework. In **Paper III**, the sulfur poisoning was carried out at 400 °C, thus, only framework-bound Cu species are expected to be present. To investigate sulfur

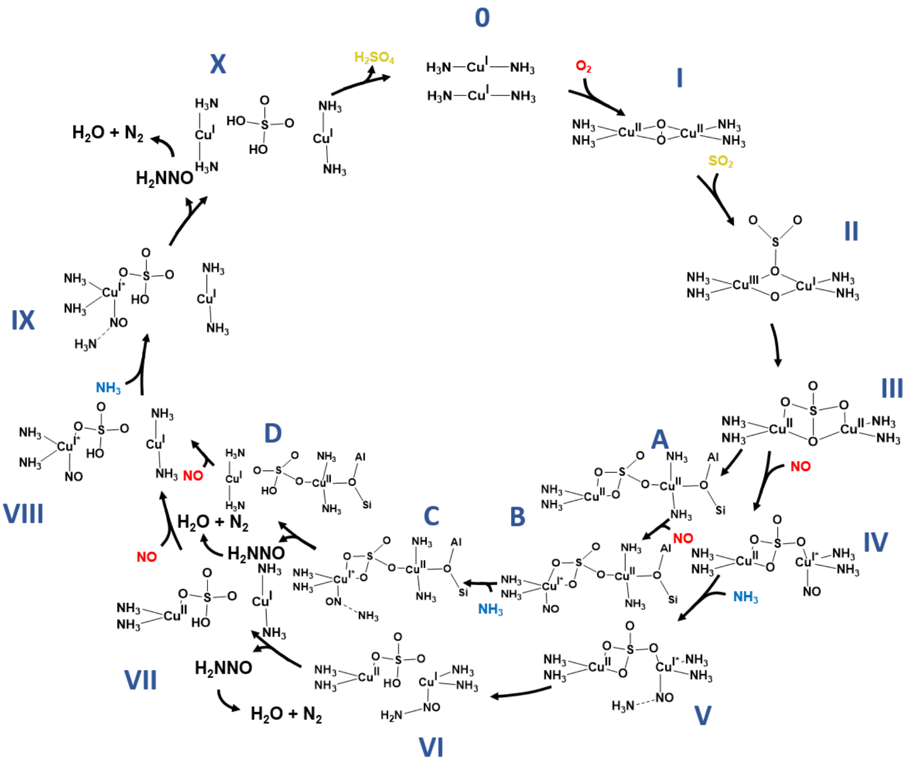
0
I
II
III
IV
V
VI
VII
VIII
IX
X
A
B
C
D
O₂
SO₂
NO
NH₃
H₂SO₄
H₂NNO
H₂O + N₂

Figure 4.2: Proposed reaction cycle for the reaction of SO_2 with $[Cu_2(NH_3)_4O_2]^{2+}$ during low-temperature NH_3-SCR conditions. Al-O-Si represents a brønsted and is only shown if the complex is bonded to the framework.

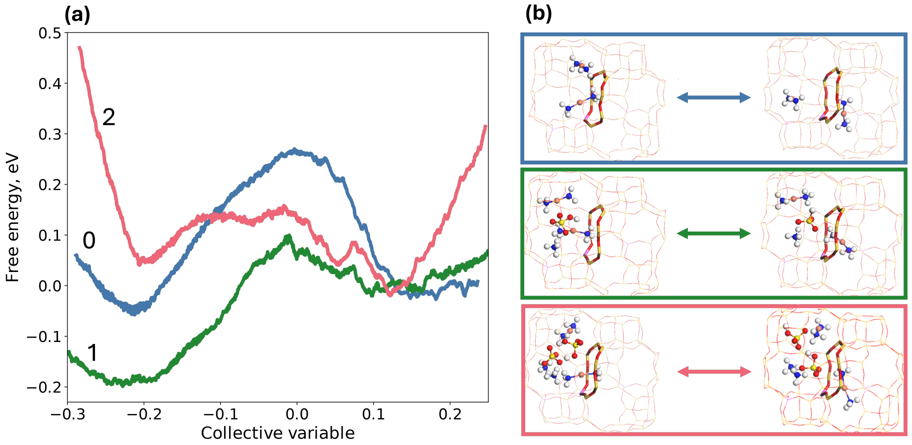

Figure 4.3: (a): Free energy profile for the diffusion of a $[Cu(NH_3)_2]$ through an eight-membered ring in the presence of a second $[Cu(NH_3)_2]^+$ and different numbers of ammonium bisulfates. (b): Snapshot of the initial and final state from the simulation.

poisoning at this temperature, the interaction with both SO_2 and SO_3 is calculated for ZCuOH, Z_2Cu, and $Z_2CuOOCu$. Framework bound Cu^+ is not found to adsorb or react with SO_x species similar to the case of $[Cu(NH_3)_2]^+$. Thus, Cu ions in oxidation state +1, are not active towards SO_2 or SO_3. Both low and high-temperature sulfur poisoning is illustrated in Figure 4.4. At low-temperature, there are the two complexes $[Cu(NH_3)_2]^+$ and $[Cu_2(NH_3)_4O_2]^{2+}$ discussed in previous section. $[Cu(NH_3)_2]^+$ can not react with SO_2, whereas $[Cu_2(NH_3)_4O_2]^{2+}$ can couple with NH_3 and NO forming $HSO_4(NH_4)$ and $[Cu_2(NH_3)_4O_2]^{2+}$ is reduced back to two $[Cu(NH_3)_2]^+$ complexes. At high temperatures, the reaction of SO_2 and SO_3 with ZCuOH leads to the formation of $ZCuHSO_3$ and $ZCuHSO_4$ respectively. The formation of $ZCuHSO_4$ is more exothermic based on the DFT calculations and associated with lower barriers, thus the reaction with SO_3 is preferred. The same trend with the reaction of SO_3 being more exothermic is calculated for Z_2Cu where SO_2 and SO_3 form $ZCuHSO_3ZH$ and $ZCuHSO_4ZH$. Note that compared to ZCuOH, a Brønsted acid (ZH) site is also formed. Comparing ZCuOH and Z_2Cu, ZCuOH is more susceptible to adsorption of sulfur as the reaction is more exothermic. The reaction of SO_x with $Z_2CuOOCu$ forms two $ZCuHSO_4$ complexes or $ZCuHSO_3$ and $ZCuHSO_4$ depending if it is exposed to a mixture of SO_2 and SO_3 or only SO_2. SO_3 alone does not react with $Z_2CuOOCu$ as the potential sulfur species would have five oxygen atoms, which is not stable. The reaction with $Z_2CuOOCu$ is more exothermic compared to both ZCuOH and Z_2Cu. In conclusion, the exposure to SO_3 forms more stable sulfur structure compared to SO_2, and the reactivity of the Cu complexes towards sulfur is in the order Z_2Cu, ZCuOH and $Z_2CuOOCu$, with $Z_2CuOOCu$ being most reactive.

The formation of Cu sulfate blocks the Cu-sites, by chemisorption, while the low-temperature deactivation is of a physical origin, where $HSO_4(NH_4)$ is formed. This fundamental difference in the poisoning mechanism may explain the large temperature effect on the sulfation of the catalyst.[98] $HSO_4(NH_4)$ is commonly assigned to the SO_2 release in TPD at 420 °C, hence, this deactivation may be recovered by heating the catalyst. However, it has been suggested that a part of the ammonium sulfate may transform to strongly bound Cu or Al sulfates.[99] The Cu sulfate formed at high temperatures is also expected to be decomposed at higher temperatures.

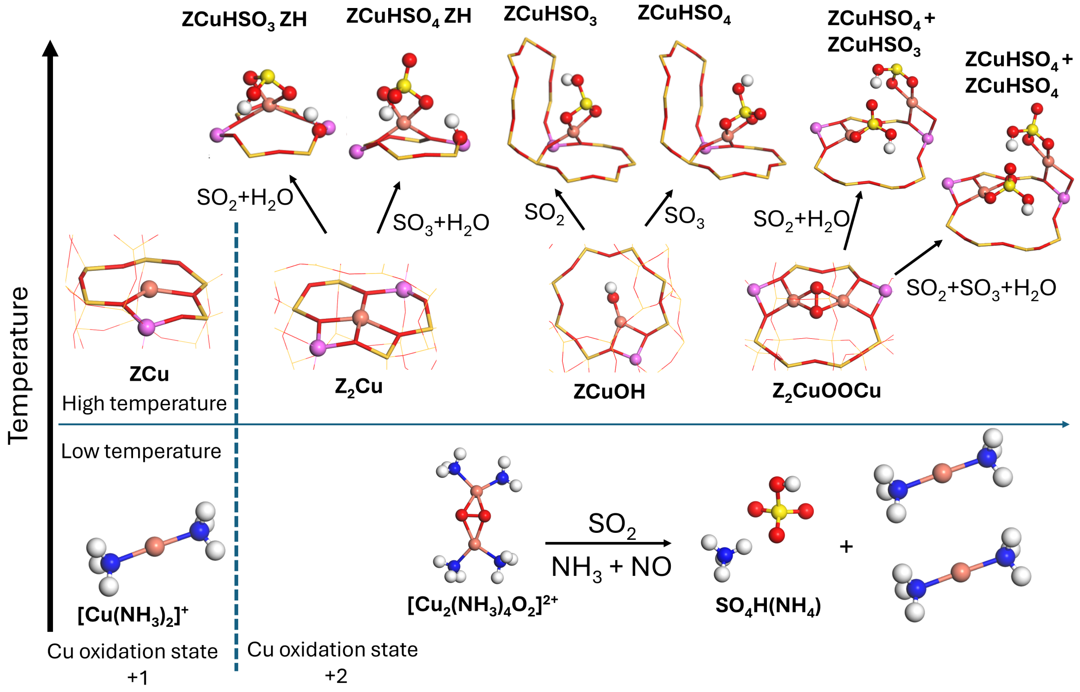
$ZCuHSO_3$ ZH
$ZCuHSO_4$ ZH
$ZCuHSO_3$
$ZCuHSO_4$
$ZCuHSO_4$ +
$ZCuHSO_3$
$ZCuHSO_4$ +
$ZCuHSO_4$
SO_2+H_2O
SO_3+H_2O
SO_2
SO_3
SO_2+H_2O
$SO_2+SO_3+H_2O$
Temperature
ZCu
High temperature
Z_2Cu
ZCuOH
$Z_2CuOOCu$
Low temperature
$[Cu(NH_3)_2]^+$
$[Cu_2(NH_3)_4O_2]^{2+}$
SO_2
NH_3 + NO
$SO_4H(NH_4)$
+
Cu oxidation state
+1
Cu oxidation state
+2

Figure 4.4: Overview of the Cu ions present at high and low temperatures for Cu oxidation state +1 and +2, together with the sulfur derived structure formed after SO_x exposure.

5

Mobility of $[Cu(NH_3)_2]^+$ Complexes

The mobility of $[Cu(NH_3)_2]^+$ complexes is important for the-low temperature NH_3-SCR since two $[Cu(NH_3)_2]^+$ complexes in the same cage are required for the adsorption of O_2. As discussed in the previous chapter, sulfur poisoning at low temperatures is related to the diffusion of $[Cu(NH_3)_2]^+$ complexes, hence, a better understanding of $[Cu(NH_3)_2]^+$ diffusion is important for further studies. The diffusion of Cu complexes is not well understood and this issue is difficult to investigate using experimental procedures. However, impedance spectroscopy has been used to track the dielectric relaxation process[100] associated with the diffusion of $[Cu(NH_3)_n]^+$, and electron paramagnetic resonance (EPR) spectroscopy to study the (super)hyperfine features which relate to the dynamics of Cu ions.[101] The conclusion from the two studies is that a higher Cu loading leads to increasing Cu mobility, and at lower Cu loadings the diffusion of Cu species becomes more important for the NH_3-SCR activity. However, the atomistic understanding of the mobility and dynamics of Cu^+ species is presently only available through computational studies. There have been several studies using ab initio molecular dynamics (AIMD) to estimate free energy barriers.[29,102] Such studies are limited to small system sizes and short simulation times. However, with the use of machine learning force field (ML-FF) it is possible to study properties otherwise inaccessible to conventional AIMD simulations. In **Paper IV**, an ML-FF is constructed to investigate the diffusion of $[Cu(NH_3)_2]^+$ in Cu-CHA. The chapter will first introduce pair correlation functions, which yield an average picture of the system, and thereafter, the mobility, and pairing are analyzed.

5.1 Pair Correlation Function

The pair correlation function (PCF) is a way to describe the environments around the atoms, by investigating the statistical distribution of distances between the atoms. In Figure 5.1(a). the PCF is shown for the Al-Cu and Al-N bonds, where N is the nitrogen in ${NH_4}^+$. For Al-Cu a broad peak at 4.5 Å is observed which corresponds to the Al atom by which the Cu is charge-stabilized. Notably, the peak has a fine structure consisting of three small peaks, related to the three different orientations Cu can have with respect to Al. For example, the last peak in the fine structure could be attributed to an Al ion at the bottom of the cage, where the repulsion from the framework hinders the $[Cu(NH_3)_2]^+$ complex from getting closer to the Al ion. Al ions located in the middle of the cage are more accessible for the

$[Cu(NH_3)_2]^+$ complex giving a shorter Al-Cu distance. Al-N has a large peak at 4 Å, which is narrower than that of Cu. This suggests that NH_4^+ does not move as much as compared to $[Cu(NH_3)_2]^+$. The smaller distance can be explained by the fact that NH_4^+ tends to stay in the center of the eight-membered ring, with the Al ion being part of the ring giving a distance of 4 Å. $[Cu(NH_3)_2]^+$ on the other hand, is moving inside the cage giving a wider peak. The two locations of $[Cu(NH_3)_2]^+$ and NH_4^+ ions are shown in Figure 5.1(c). In Figure 5.1(b), the RDFs for Cu-Cu, N-N, and Cu-N are shown. For Cu-Cu two peaks are observed, one at 5.5 Å, which is assigned to paired $[Cu(NH_3)_2]^+$ complexes, and a peak at 8 Å assigned to $[Cu(NH_3)_2]^+$ in two different cages. The lower intensity of the first peak indicates that the paired state is less stable due to repulsion between the two Cu ions. For N-N, there is a peak at 7 Å with high intensity. The distance of 7 Å corresponds to NH_4^+ ions located in two eight-membered rings next to each other. For Cu-N, no significant patterns are observed, meaning that they do not influence each other positions, which may be attributed to the fact that they occupy two different locations in the cage.

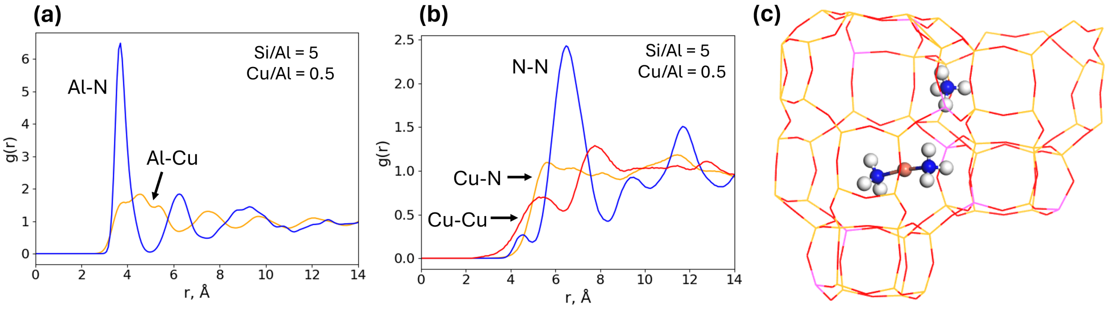

Figure 5.1: Pair correlation function for (a): Al-Cu and Al-N (b): Cu-Cu, N-N and Cu-N. Here N denotes the nitrogen atom in NH_4^+. (c): structure of Cu-CHA with the typical positions of $[Cu(NH_3)_2]^+$ and NH_4^+ ions.

5.2 Mobility and Pairing

Mean square displacement (MSD) analysis for an Si/Al ratio of 5 for $[Cu(NH_3)_2]^+$ and NH_4^+ are shown in Figure 5.2(a) and 5.2(b). Both of the ions show slow diffusion, which is a consequence of the fact that the motion is restricted by charge stabilization. Comparing $[Cu(NH_3)_2]^+$ and NH_4^+, it is clear that $[Cu(NH_3)_2]^+$ has a higher mobility as also suggested by the PCF analysis. Furthermore, a higher Cu/Al ratio enhances the diffusion of both $[Cu(NH_3)_2]^+$ and NH_4^+. This can be explained by counter diffusion where two positive counter ions change locations, retaining the charge neutrality. Since $[Cu(NH_3)_2]^+$ has a higher diffusion than NH_4^+, it can easier counter diffuse.

Figure 5.2(c) shows the fraction of paired $[Cu(NH_3)_2]^+$ complexes as a function of time for different Cu/Al ratios. A Cu/Al ratio of 0.75 exhibits the highest fraction of paired $[Cu(NH_3)_2]^+$, thus, a larger fraction of $[Cu(NH_3)_2]^+$ enhances both the mobility and pairing. The dashed line shows the fraction of paired $[Cu(NH_3)_2]^+$

complexes if they were randomly placed. For a Cu/Al ratio of 0.75 and 0.5, the simulated fraction of paired complexes is below the dashed line, indicating that the paired state is more unstable than a random distribution, probably due to the repulsion of the Cu ions. Interestingly, this is not the case for a Cu/Al ratio of 0.25 where the simulated fraction is higher than the dashed line after approximately 1 to 2 ns. The low Cu/Al ratio ratio means that there are more Al, and NH_4^+ ions per Cu ions, in this case which stabilize the paired state. Additional simulations were done with the same number of $[Cu(NH_3)_2]^+$ ions but different Si/Al ratios and these results (not shown in the Figure) indicate that more Al ions also result in a higher fraction of paired $[Cu(NH_3)_2]^+$ complexes. Figure 5.2(d) shows a histogram for the lifetime of the paired complexes $[Cu(NH_3)_2]^+$. The lifetime of the $[Cu(NH_3)_2]^+$ varies a lot from under 0.1 ns up to almost 2 ns. This suggests that some $[Cu(NH_3)_2]^+$ pairs are in a more stable position compared to others, thus, the local environments are important for the stability.

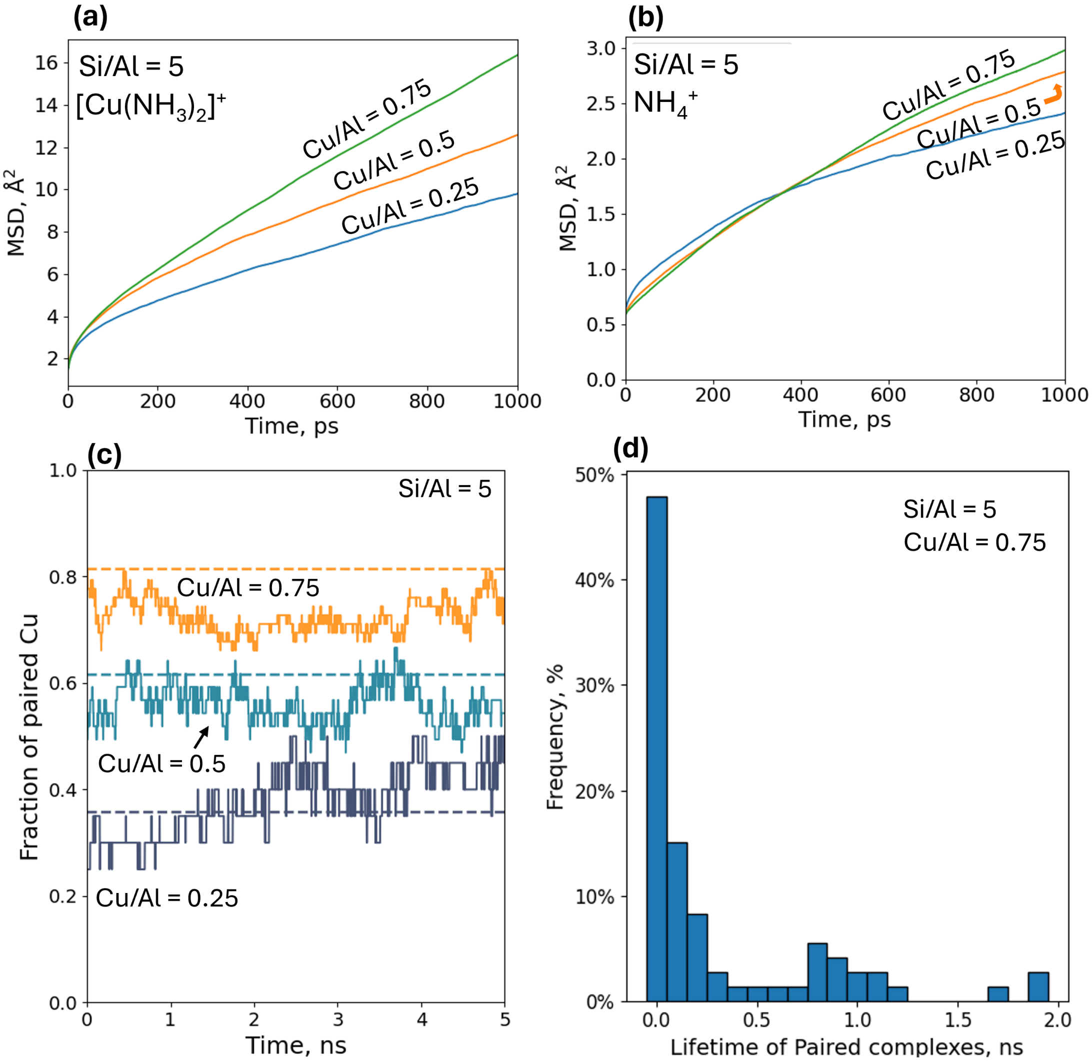

Figure 5.2: Mean square displacement (MSD) plots for (a): $[Cu(NH_3)_2]^+$ and (b): NH_3. (c): Fraction of paired $[Cu(NH_3)_2]^+$ complexes as a function of time. (d): Histogram for the lifetime of paired $[Cu(NH_3)_2]^+$ complexes.

6

Conclusions and Outlook

This thesis investigated the dynamics and reactivity of the Cu species in Cu-CHA, and the influence of sulfur species, using different theoretical methods. This includes first principle-based micro-kinetic modeling and density functional theory calculations to study H_2-TPR profiles and sulfur poisoning. To study the diffusion of Cu ions in the zeolite, a machine learning force field was constructed to enable simulations of larger systems over extended times, which was necessary to capture the diffusion dynamics.
H_2-TPR is a common technique to characterize the Cu ions in Cu-CHA, however, the interpretation is often ambiguous. To understand which Cu ions may be influencing the H_2-TPR profiles, a first-principle-based micro-kinetic model was developed. Several Cu sites in oxidation state +2 consumed H_2, which was ZCuOCu, ZCuOH, ZCuHOOHCu, Z_2Cu and ZCuOOCu. The micro-kinetic model agreed well with the experimental findings and provided a way to link Cu sites to the reduction temperatures.
The reactivity of sulfur towards Cu ions present during both-low and high-temperature NH_3-SCR conditions was studied using DFT calculations. At low temperature SO_2, was found to react strongly with the peroxo complex $[Cu_2(NH_3)_4O_2]^{2+}$. From this, a reaction mechanism was proposed involving the reaction of SO_2, NO, and NH_3, to form H_2SO_4, H_2O and N_2. As H_2SO_4 is a bulky molecule it may accumulate in the cage over time deactivating the catalyst. H_2SO_4 can interact with other NH_3 species and a thermodynamic analysis was performed that found the $HSO_4(NH_4)$ species to be most stable at typical reaction conditions. Lastly, AIMD simulations suggested that the presence of two $HSO_4(NH_4)$ species destabilizes the pairing of $[Cu(NH_3)_2]^+$, inhibiting the adsorption of O_2. The reaction of SO_2 and SO_3 towards the framework-bound Cu complexes Z_2Cu, ZCuOH and ZCuOOCu present at high temperature, showed that more stable Cu sulfates were formed when reacting with SO_3. ZCuOH and ZCuOOCu form more stable Cu sulfur complexes compared to Z_2Cu. The two studies show that there is a large difference in the poisoning mechanism depending the temperature. At low temperatures, the poisoning mechanism is physical blocking by the accumulation of $HSO_4(NH_4)$ species, while at high temperatures, the Cu sites are blocked by forming stable Cu sulfites/sulfates.

Lastly, a machine learning force-field was constructed to study the mobility and pairing of $[Cu(NH_3)_2]^+$ complexes by varying the zeolite composition (Si/Al and Cu/Al). The mobility of both $[Cu(NH_3)_2]^+$ and $NH_4{}^+$ ions is enhanced by increasing Cu/Al ratio, which is attributed to increased counter diffusion. A lower Si/Al ratio decreases the mobility since the $NH_4{}^+$ prefer to stay in the eight-membered ring effectively blocking other ions from diffusion. The fraction of paired $[Cu(NH_3)_2]^+$ complexes is enhanced by increasing the Cu/Al ratio and decreasing the Si/Al ratio. Interestingly, if there is a high amount of Al and $NH_4{}^+$ ions, the simulated fraction of paired $[Cu(NH_3)_2]^+$ complexes is higher than if they were randomly put. By using machine learning force-field this study gives information on the diffusion dynamics of $[Cu(NH_3)_2]^+$ and the interplay between the Al ions and counter ions otherwise inaccessible to conventional AIMD simulations.

This thesis has proposed mechanisms on how SO_x may deactivate the catalyst at both high and low temperatures, however, there are still important questions that remain unanswered. Firstly, how the two different kinds of Cu species formed during the two temperature regimes are connected. The possible interconversion between $HSO_4(NH_4)$ and Cu sulfate may play an important role in the stability of the sulfur species and should be investigated. The low-temperature deactivation is linked to the destabilization of paired $[Cu(NH_3)_2]^+$ complexes, however, this has only been studied using small unit cells with short simulation times. To study how $HSO_4(NH_4)$ species influence the pairing of $[Cu(NH_3)_2]^+$ complexes, the machine learning force-field constructed in this thesis could be extended to allow simulation containing sulfur species.

The use of machine learning force-fields allows simulation in the range of nano-seconds, however, turnover frequencies typically occur at much longer timescales. To extend simulation times, a kinetic Monte Carlo model can be used. This method requires knowledge of rates concerning the diffusion of Cu species, which may be derived using the machine learning force-field.

Acknowledgements

The research was carried out at the Division of Chemical Physics and Competence Centre for Catalysis at Chalmers University of Technology, Göteborg, Sweden, and at Umicore AG & Co. KG, Hanau, Germany in the period October 2021 to January 2024.

The research is funded by the European Union's Horizon 2020 research and innovation programme under the Marie Sklodowska-Curie grant agreement no. 955839 (CHASS), with additional support from the Swedish Energy Agency (47110-1).

The Competence Centre for Catalysis is hosted by Chalmers University of Technology, and financially supported by the Swedish Energy Agency, and the member companies: AB Volvo, ECAPS AB, Johnson Matthey AB, Preem AB, Scania CV AB, and Umicore Denmark Aps.

Computational time was granted by SNIC at C3SE (Göteborg), PDC (Stockholm) and NSC (Linköping).

In addition, I want to thank:

My main supervisor, Henrik Grönbeck. Thank you for your guidance and support and for always being available for discussions.

My co-supervisor Martin Votsmeier for discussions and advice on my research.

The members of the CHASS project, for the valuable discussions and ideas. It is always a pleasure to attend our project meetings.

All colleagues at both Chemical Physics and Umicore for creating a good working environment.

Lastly, I would like to thank my family and friends for always supporting me.

Bibliography

1. Collins, W. D., Ramaswamy, V., Schwarzkopf, M. D., Sun, Y., Portmann, R. W., Fu, Q., Casanova, S. E. B., Dufresne, J.-L., Fillmore, D. W., Forster, P. M. D., Galin, V. Y., Gohar, L. K., Ingram, W. J., Kratz, D. P., Lefebvre, M.-P., Li, J., Marquet, P., Oinas, V., Tsushima, Y., Uchiyama, T. & Zhong, W. Y. Radiative Forcing by Well-Mixed Greenhouse Gases: Estimates from Climate Models in the Intergovernmental Panel on Climate Change (IPCC) Fourth Assessment Report (AR4). *J. Geophys. Res.: Atmos.* **111** (2006).
2. Health organization, W. WHO Global air quality guidelines. Particulate matter ($PM_{2.5}$ and PM_{10}), ozone, nitrogen oxide, sulfur dioxide and carbon monoxide. (ed Organization, W. H.) (2021).
3. Skalska, K., Miller, J. S. & Ledakowicz, S. Trends in NO Abatement: A Review. *Sci. Total Environ.* **408,** 3976–3989 (2010).
4. European Environment Agency. *Air Quality in Europe: 2019 Report.* (Publications Office, LU, 2019).
5. Selleri, T., Melas, A. D., Joshi, A., Manara, D., Perujo, A. & Suarez-Bertoa, R. An Overview of Lean Exhaust deNOx Aftertreatment Technologies and NOx Emission Regulations in the European Union. *Catal.* **11,** 404 (2021).
6. Atkinson, R. Atmospheric Chemistry of VOCs and NOV. *Atmospheric Environment* (2000).
7. Hasager, F., Bjerregaard, J. D., Bonomaully, J., Knap, H., Afshari, A. & Johnson, M. S. in *Air Pollution Sources, Statistics and Health Effects* 135–162 (Springer US, 2021).
8. Abbasi, T., Poornima, P., Kannadasan, T. & Abbasi, S. Acid Rain: Past, Present, and Future. *Int. J. Environ. Eng.* **5,** 229–272 (2013).
9. Wang, J., Chen, H., Hu, Z., Yao, M. & Li, Y. A Review on the Pd-Based Three-Way Catalyst. *Catal. Rev.* **57,** 79–144 (2015).
10. Miyoshi, N., Matsumoto, S., Katoh, K., Tanaka, T., Harada, J., Takahashi, N., Yokota, K., Sugiura, M. & Kasahara, K. Development of New Concept Three-Way Catalyst for Automotive Lean-Burn Engines. *SAE trans.* **104,** 1361–1370 (1995).
11. Damma, D., Ettireddy, P. R., Reddy, B. M. & Smirniotis, P. G. A Review of Low Temperature NH_3-SCR for Removal of NOx. *Catal.* **9,** 349 (2019).
12. International Union of Pure and Applied Chemistry (IUPAC) (2019).
13. Heveling, J. Heterogeneous Catalytic Chemistry by Example of Industrial Applications. *J. Chem. Educ.* **89,** 1530–1536 (2012).
14. Bertini, I. *Inorganic and Bio-Inorganic Chemistry - Volume II* (2009).

15. Argyle, M. D. & Bartholomew, C. H. Heterogeneous Catalyst Deactivation and Regeneration: A Review. *Catal.* **5,** 145–269 (2015).
16. Jeon, J., Lee, J. T. & Park, S. Nitrogen Compounds (NO, NO_2, N_2O, and NH_3) in NO_x Emissions from Commercial EURO VI Type Heavy-Duty Diesel Engines with a Urea-Selective Catalytic Reduction System. *Energy Fuels* **30,** 6828–6834 (2016).
17. Zhang, J., Li, X., Chen, P. & Zhu, B. Research Status and Prospect on Vanadium-Based Catalysts for NH_3-SCR Denitration. *Materials* **11,** 1632 (2018).
18. Chen, H., Xia, Y., Fang, R., Huang, H., Gan, Y., Liang, C., Zhang, J., Zhang, W. & Liu, X. The Effects of Tungsten and Hydrothermal Aging in Promoting NH_3-SCR Activity on V_2O_5/WO_3-TiO_2 Catalysts. *Appl. Surf. Sci.* **459,** 639–646 (2018).
19. Schildhauer, T. J., Elsener, M., Moser, J., Begsteiger, I., Chatterjee, D., Rusch, K. & Kröcher, O. Measurement of Vanadium Emissions from SCR Catalysts by ICP-OES: Method Development and First Results. *Emiss. Control Sci. Technol.* **1,** 292–297 (2015).
20. Zhu, M., Lai, J.-K., Tumuluri, U., Ford, M. E., Wu, Z. & Wachs, I. E. Reaction Pathways and Kinetics for Selective Catalytic Reduction (SCR) of Acidic NO_x Emissions from Power Plants with NH_3. *ACS Catal.* **7,** 8358–8361 (2017).
21. Davis, M. E. & Lobo, R. F. Zeolite and Molecular Sieve Synthesis. *Chem. Mater.* **4,** 756–768 (1992).
22. Xin, Y., Li, Q. & Zhang, Z. Zeolitic Materials for DeNO_x Selective Catalytic Reduction. *ChemCatChem* **10,** 29–41 (2018).
23. *IZA Structure Commission* `http://www.iza-structure.org/` (2024).
24. Auvray, X., Arvanitidou, M., Högström, Å., Jansson, J., Fouladvand, S. & Olsson, L. Comparative Study of SO_2 and SO_2/SO_3 Poisoning and Regeneration of Cu/BEA and Cu/SSZ-13 for NH_3 SCR. *Emiss. Control Sci. Technol.* **7,** 232–246 (2021).
25. Wilken, N., Wijayanti, K., Kamasamudram, K., Currier, N. W., Vedaiyan, R., Yezerets, A. & Olsson, L. Mechanistic Investigation of Hydrothermal Aging of Cu-Beta for Ammonia SCR. *Appl. Catal. B* **111,** 58–66 (2011).
26. Luo, J.-Y., Oh, H., Henry, C. & Epling, W. Effect of C_3H_6 on Selective Catalytic Reduction of NOx by NH_3 over a Cu/Zeolite Catalyst: A Mechanistic Study. *Appl. Catal. B* **123–124,** 296–305 (2012).
27. Schmieg, S. J., Oh, S. H., Kim, C. H., Brown, D. B., Lee, J. H., Peden, C. H. F. & Kim, D. H. Thermal Durability of Cu-CHA NH_3-SCR Catalysts for Diesel NOx Reduction. *Catal. Today* **184,** 252–261 (2012).
28. Kwak, J. H., Tonkyn, R. G., Kim, D. H., Szanyi, J. & Peden, C. H. F. Excellent Activity and Selectivity of Cu-SSZ-13 in the Selective Catalytic Reduction of NOx with NH_3. *J. Catal.* **275,** 187–190 (2010).
29. Paolucci, C., Khurana, I., Parekh, A. A., Li, S., Shih, A. J., Li, H., Di Iorio, J. R., Albarracin-Caballero, J. D., Yezerets, A., Miller, J. T., Delgass, W. N., Ribeiro, F. H., Schneider, W. F. & Gounder, R. Dynamic Multinuclear Sites Formed by Mobilized Copper Ions in NOx Selective Catalytic Reduction. *Science* **357,** 898–903 (2017).

30. Chen, L., Janssens, T. V. W., Vennestrøm, P. N. R., Jansson, J., Skoglundh, M. & Grönbeck, H. A Complete Multisite Reaction Mechanism for Low-Temperature NH_3-SCR over Cu-CHA. *ACS Catal.* **10,** 5646–5656 (2020).
31. Feng, Y., Wang, X., Janssens, T. V. W., Vennestrøm, P. N. R., Jansson, J., Skoglundh, M. & Grönbeck, H. First-Principles Microkinetic Model for Low-Temperature NH_3-Assisted Selective Catalytic Reduction of NO over Cu-CHA. *ACS Catal.* **11,** 14395–14407 (2021).
32. Shan, Y., Du, J., Zhang, Y., Shan, W., Shi, X., Yu, Y., Zhang, R., Meng, X., Xiao, F.-S. & He, H. Selective Catalytic Reduction of NO_x with NH_3: Opportunities and Challenges of Cu-based Small-Pore Zeolites. *Natl. Sci. Rev.* **8,** nwab010 (2021).
33. Xie, K., Leistner, K., Wijayanti, K., Kumar, A., Kamasamudram, K. & Olsson, L. Influence of Phosphorus on Cu-SSZ-13 for Selective Catalytic Reduction of NO_x by Ammonia. *Catal. Today* **297**, 46–52 (2017).
34. Guo, J., Wang, A. & Lin, H. Effect of Phosphorus Poisoning on the Hydrothermal Stability of Cu/CHA and Cu/LTA towards NH_3-SCR. *Microporous Mesoporous Mater.* **346,** 112313 (2022).
35. Luo, J.-Y., Yezerets, A., Henry, C., Hess, H., Kamasamudram, K., Chen, H.-Y. & Epling, W. S. Hydrocarbon Poisoning of Cu-Zeolite SCR Catalysts. *SAE Tech. Pap.* **1,** 1096 (2012).
36. Gao, F. & Szanyi, J. On the Hydrothermal Stability of Cu/SSZ-13 SCR Catalysts. *Appl. Catal. A Gen.* **560,** 185–194 (2018).
37. Cheng, Y., Montreuil, C., Cavataio, G. & Lambert, C. Sulfur Tolerance and $DeSO_x$ Studies on Diesel SCR Catalysts. *SAE Int. J. Fuels Lubr.* **1,** 471–476 (2008).
38. Hammershøi, P. S., Jensen, A. D. & Janssens, T. V. W. Impact of SO_2-poisoning over the Lifetime of a Cu-CHA Catalyst for NH_3-SCR. *Appl. Catal. B* **238,** 104–110 (2018).
39. Bjerregaard, J. D., Votsmeier, M. & Grönbeck, H. Mechanism for SO_2 Poisoning of Cu-CHA during Low Temperature NH_3-SCR. *J. Catal.* **417,** 497–506 (2023).
40. Hammershøi, P. S., Jangjou, Y., Epling, W. S., Jensen, A. D. & Janssens, T. V. W. Reversible and Irreversible Deactivation of Cu-CHA NH_3-SCR catalysts by SO_2 and SO_3. *Appl. Catal. B* **226,** 38–45 (2018).
41. Jia, L., Liu, J., Huang, D., Zhao, J., Zhang, J., Li, K., Li, Z., Zhu, W., Zhao, Z. & Liu, J. Interface Engineering of a Bifunctional Cu-SSZ-13@CZO Core–Shell Catalyst for Boosting Potassium Ion and SO_2 Tolerance. *ACS Catal.* **18,** 11281–11293 (2022).
42. Paolucci, C., Parekh, A. A., Khurana, I., Di Iorio, J. R., Li, H., Albarracin Caballero, J. D., Shih, A. J., Anggara, T., Delgass, W. N., Miller, J. T., Ribeiro, F. H., Gounder, R. & Schneider, W. F. Catalysis in a Cage: Condition-Dependent Speciation and Dynamics of Exchanged Cu Cations in SSZ-13 Zeolites. *J. Am. Chem. Soc.* **138,** 6028–6048 (2016).
43. Hartree, D. R. The Wave Mechanics of an Atom with a Non-Coulomb Central Field. Part II. Some Results and Discussion. *Math. Proc. Cambridge Philos. Soc.* **24,** 111–132 (1928).

44. Fock, V. Näherungsmethode zur Lösung des quantenmechanischen Mehrkörperproblems. *Zeitschrift für Physik* **61,** 126–148 (1930).
45. Hohenberg, P. & Kohn, W. Inhomogeneous Electron Gas. *Phys. Rev.* **136,** B864–B871 (1964).
46. Kohn, W. & Sham, L. J. Self-Consistent Equations Including Exchange and Correlation Effects. *Phys. Rev.* **140,** A1133–A1138 (1965).
47. Ceperley, D. M. & Alder, B. J. Ground State of the Electron Gas by a Stochastic Method. *Phys. Rev. Lett.* **45,** 566–569 (1980).
48. Cohen, A. J., Mori-Sánchez, P. & Yang, W. Challenges for Density Functional Theory. *Chem. Rev.,* 289–320 (2012).
49. Perdew, J. P., Burke, K. & Ernzerhof, M. Generalized Gradient Approximation Made Simple. *Phys. Rev. Lett.* **77,** 3865–3868 (1996).
50. Jensen, F. *Introduction to Computational Chemistry* 3rd. 638 pp. ISBN: 978-1-118-82599-0 (Wiley, 2017).
51. Becke, A. D. A New Mixing of Hartree–Fock and Local Density-functional Theories. *J. Chem. Phys.* **98,** 1372–1377 (1993).
52. Lee, C., Yang, W. & Parr, R. G. Development of the Colle-Salvetti Correlation-Energy Formula into a Functional of the Electron Density. *Phys. Rev. B* **37,** 785–789 (1988).
53. Dudarev, S. L., Botton, G. A., Savrasov, S. Y., Humphreys, C. J. & Sutton, A. P. Electron-Energy-Loss Spectra and the Structural Stability of Nickel Oxide: An LSDA+U Study. *Phys. Rev. B* **57,** 1505–1509 (1998).
54. Arovas, D. P., Berg, E., Kivelson, S. A. & Raghu, S. The Hubbard Model. *Annu. Rev. Condens. Matter Phys.* **13,** 239–274 (2022).
55. Grimme, S., Antony, J., Ehrlich, S. & Krieg, H. A Consistent and Accurate Ab Initio Parametrization of Density Functional Dispersion Correction (DFT-D) for the 94 Elements H-Pu. *J. Chem. Phys.* **132,** 154104 (2010).
56. Blöchl, P. E. Projector Augmented-Wave Method. *Phys. Rev. B* **50,** 17953–17979 (1994).
57. Tang, W., Sanville, E. & Henkelman, G. A Grid-Based Bader Analysis Algorithm without Lattice Bias. *J. Phys.: Condens. Matter* **21,** 084204 (2009).
58. Yu, M. & Trinkle, D. R. Accurate and Efficient Algorithm for Bader Charge Integration. *J. Chem. Phys.* **134,** 064111 (2011).
59. Ponder, J. W. & Case, D. A. in *Advances in Protein Chemistry* 27–85 (2003).
60. Krieger, E., Darden, T., Nabuurs, S. B., Finkelstein, A. & Vriend, G. Making Optimal Use of Empirical Energy Functions: Force-field Parameterization in Crystal Space. *Proteins Struct. Funct. Bioinf.* **57,** 678–683 (2004).
61. Case, D. A., Cheatham III, T. E., Darden, T., Gohlke, H., Luo, R., Merz Jr., K. M., Onufriev, A., Simmerling, C., Wang, B. & Woods, R. J. The Amber Biomolecular Simulation Programs. *J. Comput. Chem.* **26,** 1668–1688 (2005).
62. Rappe, A. K., Casewit, C. J., Colwell, K. S., Goddard, W. A. I. & Skiff, W. M. UFF, a Full Periodic Table Force Field for Molecular Mechanics and Molecular Dynamics Simulations. *J. Am. Chem. Soc.* **114,** 10024–10035 (1992).
63. Unke, O. T., Chmiela, S., Sauceda, H. E., Gastegger, M., Poltavsky, I., Schütt, K. T., Tkatchenko, A. & Müller, K.-R. Machine Learning Force Fields. *Chem. Rev.* **121,** 10142–10186 (2021).

64. Van Duin, A. C. T., Dasgupta, S., Lorant, F. & Goddard, W. A. ReaxFF: A Reactive Force Field for Hydrocarbons. *J. Phys. Chem. A* **105,** 9396–9409 (2001).
65. Senftle, T. P., Hong, S., Islam, M. M., Kylasa, S. B., Zheng, Y., Shin, Y. K., Junkermeier, C., Engel-Herbert, R., Janik, M. J., Aktulga, H. M., Verstraelen, T., Grama, A. & van Duin, A. C. T. The ReaxFF Reactive Force-Field: Development, Applications and Future Directions. *npj Comput. Mater.* **2,** 1–14 (2016).
66. Anstine, D. M. & Isayev, O. Machine Learning Interatomic Potentials and Long-Range Physics. *J. Phys. Chem. A* **127,** 2417–2431 (2023).
67. Zhang, L., Wang, H., Muniz, M. C., Panagiotopoulos, A. Z., Car, R. & E, W. A Deep Potential Model with Long-Range Electrostatic Interactions. *J. Chem. Phys.* **156,** 124107 (2022).
68. Zhang, L., Han, J., Wang, H., Car, R. & E, W. Deep Potential Molecular Dynamics: A Scalable Model with the Accuracy of Quantum Mechanics. *Phys. Rev. Lett.* **120,** 143001 (2018).
69. Keith, J. A., Vassilev-Galindo, V., Cheng, B., Chmiela, S., Gastegger, M., Müller, K.-R. & Tkatchenko, A. Combining Machine Learning and Computational Chemistry for Predictive Insights Into Chemical Systems. *Chem. Rev.* **121,** 9816–9872 (2021).
70. Henkelman, G. & Jónsson, H. Improved Tangent Estimate in the Nudged Elastic Band Method for Finding Minimum Energy Paths and Saddle Points. *J. Chem. Phys.* **113,** 9978–9985 (2000).
71. Henkelman, G., Uberuaga, B. P. & Jónsson, H. A Climbing Image Nudged Elastic Band Method for Finding Saddle Points and Minimum Energy Paths. *J. Chem. Phys.* **113,** 9901–9904 (2000).
72. Lucas, K. *Applied Statistical Thermodynamics* 529 pp. ISBN: 978-3-662-01648-0 (Springer Science & Business Media, 2013).
73. Jørgensen, M., Chen, L. & Grönbeck, H. Monte Carlo Potential Energy Sampling for Molecular Entropy in Zeolites. *J. Phys. Chem. C* **122,** 20351–20357 (2018).
74. Swope, W. C., Andersen, H. C., Berens, P. H. & Wilson, K. R. A Computer Simulation Method for the Calculation of Equilibrium Constants for the Formation of Physical Clusters of Molecules: Application to Small Water Clusters. *J. Chem. Phys.* **76,** 637–649 (1982).
75. Nosé, S. A Unified Formulation of the Constant Temperature Molecular Dynamics Methods. *J. Chem. Phys.* **81,** 511–519 (1984).
76. Hoover, W. G. Canonical Dynamics: Equilibrium Phase-Space Distributions. *Phys. Rev. A* **31,** 1695–1697 (1985).
77. Branduardi, D., Gervasio, F. L. & Parrinello, M. From A to B in Free Energy Space. *J. Chem. Phys.* **126,** 054103 (2007).
78. Woo, T. K., Margl, P. M., Blöchl, P. E. & Ziegler, T. A Combined Car Parrinello QM/MM Implementation for Ab Initio Molecular Dynamics Simulations of Extended Systems: Application to Transition Metal Catalysis. *J. Phys. Chem. B* **101,** 7877–7880 (1997).

79. Barducci, A., Bussi, G. & Parrinello, M. Well-Tempered Metadynamics: A Smoothly Converging and Tunable Free-Energy Method. *Phys. Rev. Lett.* **100,** 020603 (2008).
80. Carter, E. A., Ciccotti, G., Hynes, J. T. & Kapral, R. Constrained Reaction Coordinate Dynamics for the Simulation of Rare Events. *Phys. Rev. Lett.* **156,** 472–477 (1989).
81. Laio, A. & Parrinello, M. Escaping Free-Energy Minima. *Proc. Natl. Acad. Sci.* **99,** 12562–12566 (2002).
82. Sutto, L., Marsili, S. & Gervasio, F. L. New Advances in Metadynamics. *WIREs Comput. Mol. Sci.* **2,** 771–779 (2012).
83. Motagamwala, A. H. & Dumesic, J. A. Microkinetic Modeling: A Tool for Rational Catalyst Design. *Chem. Rev.* **121,** 1049–1076 (2021).
84. Zhang, Y., Peng, Y., Li, J., Groden, K., McEwen, J.-S., Walter, E. D., Chen, Y., Wang, Y. & Gao, F. Probing Active-Site Relocation in Cu/SSZ-13 SCR Catalysts during Hydrothermal Aging by In Situ EPR Spectroscopy, Kinetics Studies, and DFT Calculations. *ACS Catal.* **10,** 9410–9419 (2020).
85. Gao, F., Washton, N. M., Wang, Y., Kollár, M., Szanyi, J. & Peden, C. H. F. Effects of Si/Al Ratio on Cu/SSZ-13 NH_3-SCR Catalysts: Implications for the Active Cu Species and the Roles of Brønsted Acidity. *J. Catal.* **331,** 25–38 (2015).
86. Jangjou, Y., Do, Q., Gu, Y., Lim, L.-G., Sun, H., Wang, D., Kumar, A., Li, J., Grabow, L. C. & Epling, W. S. Nature of Cu Active Centers in Cu-SSZ-13 and Their Responses to SO_2 Exposure. *ACS Catal.* **8,** 1325–1337 (2018).
87. Han, J., Wang, A., Isapour, G., Härelind, H., Skoglundh, M., Creaser, D. & Olsson, L. N_2O Formation during NH_3-SCR over Different Zeolite Frameworks: Effect of Framework Structure, Copper Species, and Water. *Ind. Eng. Chem. Res.* **60,** 17826–17839 (2021).
88. Gao, F., Walter, E. D., Karp, E. M., Luo, J., Tonkyn, R. G., Kwak, J. H., Szanyi, J. & Peden, C. H. F. Structure–Activity Relationships in NH_3-SCR over Cu-SSZ-13 as Probed by Reaction Kinetics and EPR Studies. *J. Catal.* **300,** 20–29 (2013).
89. Nielsen, D., Gao, Q., Janssens, T. V. W., Vennestrøm, P. N. R. & Mossin, S. Cu-Speciation in Dehydrated CHA Zeolites Studied by H_2-TPR and In Situ EPR. *J. Phys. Chem. C* **127,** 12995–13004 (2023).
90. Kwak, J. H., Zhu, H., Lee, J. H., Peden, C. H. F. & Szanyi, J. Two Different Cationic Positions in Cu-SSZ-13? *Chem. Commun.* **48,** 4758–4760 (2012).
91. Lomachenko, K., Borfecchia, E., Negri, C., Berlier, G., Lamberti, C., Beato, P., Falsig, H. & Bordiga, S. The Cu-CHA deNO$_x$ Catalyst in Action: Temperature-Dependent NH_3-Assisted Selective Catalytic Reduction Monitored by Operando XAS and XES. *J. Am. Chem. Soc.* **138,** 12025–12028 (2016).
92. Ipek, B., Wulfers, M. J., Kim, H., Göltl, F., Hermans, I., Smith, J. P., Booksh, K. S., Brown, C. M. & Lobo, R. F. Formation of $[Cu_2O_2]^{2+}$ and $[Cu_2O]^{2+}$ toward C–H Bond Activation in Cu-SSZ-13 and Cu-SSZ-39. *ACS Catal.* **7,** 4291–4303 (2017).
93. Rhoda, H. M., Plessers, D., Heyer, A. J., Bols, M. L., Schoonheydt, R. A., Sels, B. F. & Solomon, E. I. Spectroscopic Definition of a Highly Reactive Site

in Cu-CHA for Selective Methane Oxidation: Tuning a Mono-μ-Oxo Dicopper(II) Active Site for Reactivity. *J. Am. Chem. Soc.* **143,** 7531–7540 (2021).

94. Bregante, D. T., Wilcox, L. N., Liu, C., Paolucci, C., Gounder, R. & Flaherty, D. W. Dioxygen Activation Kinetics over Distinct Cu Site Types in Cu-Chabazite Zeolites. *ACS Catal.* **11,** 11873–11884 (2021).
95. Fahami, A. R., Günter, T., Doronkin, D. E., Casapu, M., Zengel, D., Vuong, T. H., Simon, M., Breher, F., Kucherov, A. V., Brückner, A., *et al.* The Dynamic Nature of Cu Sites in Cu-SSZ-13 and the Origin of the Seagull NOx Conversion Profile during NH_3-SCR. *React. Chem. Eng.* **4,** 1000–1018 (2019).
96. Wijayanti, K., Xie, K., Kumar, A., Kamasamudram, K. & Olsson, L. Effect of Gas Compositions on SO_2 Poisoning over Cu/SSZ-13 Used for NH_3-SCR. *Appl. Catal., B* **219,** 142–154 (2017).
97. Xi, Y., Ottinger, N., Su, C. & Liu, Z. G. Sulfur Poisoning of a Cu-SSZ-13 SCR Catalyst under Simulated Diesel Engine Operating Conditions. *SAE Int. J. Adv. Curr. Pract. Mobil.* **3,** 2690–2694 (2021).
98. Yao, D., Hu, X., Li, Y., Hu, J., He, H., Wang, L., Jin, W. & Wu, F. Experimental Study on the Effects of the Exhaust Atmosphere on SO_2 Poisoning over the Cu-SSZ-13 SCR Catalyst. *Energy Fuels* (2023).
99. Mesilov, V., Dahlin, S., Bergman, S. L., Xi, S., Han, J., Olsson, L., Pettersson, L. J. & Bernasek, S. L. Regeneration of Sulfur-Poisoned Cu-SSZ-13 Catalysts: Copper Speciation and Catalytic Performance Evaluation. *Appl. Catal. B* **299,** 120626 (2021).
100. Rizzotto, V., Chen, P. & Simon, U. Mobility of NH_3-Solvated Cu^{II} Ions in Cu-SSZ-13 and Cu-ZSM-5 NH_3-SCR Catalysts: A Comparative Impedance Spectroscopy Study. *Catal.* **8,** 162 (2018).
101. Wu, Y., Ma, Y., Wang, Y., Rappé, K. G., Washton, N. M., Wang, Y., Walter, E. D. & Gao, F. Rate Controlling in Low-Temperature Standard NH_3-SCR: Implications from Operando EPR Spectroscopy and Reaction Kinetics. *J. Am. Chem. Soc.* **144,** 9734–9746 (2022).
102. Millan, R., Cnudde, P., van Speybroeck, V. & Boronat, M. Mobility and Reactivity of Cu^+ Species in Cu-CHA Catalysts under NH_3-SCR-NOx Reaction Conditions: Insights from AIMD Simulations. *JACS Au* **1,** 1778–1787 (2021).